

Analytical perils (and progress) in electron microprobe trace element analysis applied to geochronology: Background acquisition, interferences, and beam irradiation effects

MICHAEL J. JERCINOVIC* AND MICHAEL L. WILLIAMS

Department of Geosciences, University of Massachusetts, 611 North Pleasant Street, Amherst, Massachusetts 01003, U.S.A.

ABSTRACT

Electron probe microanalysis (EPMA) of accessory minerals such as monazite, xenotime, and thorite for minor- and trace-element concentrations and geochronology, requires consideration of beam irradiation effects (increasing heat and charge) as higher current densities and lengthy counting times are employed, and requires careful, detailed assessment of background intensities and interferences. A carbon coat (250 Å thickness) is generally inadequate for prevention of absorbed current fluctuation and beam damage when using the high current densities applied for high precision (e.g., 200 nA, focused beam). Beam irradiation effects include element mobility in monazite, resulting in P loss relative to REE. Coating materials of higher electrical and thermal conductivity are indicated, and use of gold (≥ 100 Å) is strongly suggested. Systematic compositional and, therefore, age variability can result simply from analytical effects, requiring evaluation of all aspects of data acquisition. The spectra relevant to measurement of Y, Th, Pb, and U are complex, especially in REE-bearing minerals. Acquisition of detailed spectral wavelength scans allows recognition of background and peak interferences, as well as curvature. Background intensities can be extracted directly from scan data by regression. X-ray mapping allows delineation of domains, guiding background acquisition and detailed quantitative analysis. Minor substitution or fluorescence of unexpected elements can compromise analyses, one documented effect being the fluorescence of K in monazite adjacent to, or hosted by, K-feldspar or micas. This effect, clearly evident within 10 micrometers from K-feldspar, can result in erroneous U concentrations leading to misinterpretation of rim “ages” as younger overgrowths. Absorption edges associated with Th also become relevant to the measurement of U at high Th concentrations. Because background intensity is sensitive to variation in average atomic number, backgrounds must be acquired from each identified domain, with particular attention being paid to Th variation. Misapplication of background intensities can result in large age discrepancies, for example, application of backgrounds obtained from a high-Th domain in monazite to measurement of a low-Th domain (1/3 of the amount in the high-Th domain) results in an overestimation of the $UM\beta$ background intensity of 0.008 cps/nA, and an overall “increase” in age of 70 m.y.

INTRODUCTION

Modern electron microprobes are increasingly automated, making identification of mineral grains and analytical setup convenient, straightforward, and relatively rapid. However, the accessibility and familiarity of the microprobe may also lead to problems. It is tempting to apply the same methods to trace-element analysis and geochronology as have been successful for major-element analyses and to have the same expectations. However, trace-element analyses and geochronologic calculations involve significant challenges not faced in major-element analysis including: (1) The total electron dose to the specimen during trace analysis can be at least two orders-of-magnitude greater than typically applied for major-element analysis, with complicating electrical and thermal effects; (2) Peak to background ratios (P/B) are commonly extremely small, requiring a detailed understanding of background characteristics and very accurate background measurement; and (3) Even exceptionally minor contributions

from both peak and background interferences can dramatically influence results, and produce large errors in estimated age. Many features that “disappear into the background” at high P/B ratios, can have major manifestations in acquired trace-element concentrations and resulting age estimates.

The purpose of this paper is to summarize the results of an investigation of several components of the trace element-microprobe geochronologic analytical procedure, particularly the analysis of the trace or minor elements Th, U, and Pb, in monazite. In particular, we focus on three critical components of the analytical procedure: (1) sample preparation and coating, (2) background analysis, and (3) the characterization of, and correction for, elemental interferences. Several other considerations are more briefly discussed. In the end, we present suggestions for an analytical procedure for monazite geochronologic analysis. Although our focus is specifically on geochronology, these considerations are relevant to most trace-element analyses on the electron microprobe. Improvements and refinements of both hardware and software on modern electron microprobes are beginning to show that the potential for high-resolution

* E-mail: mjj@geo.umass.edu

and accurate trace-element analysis can be realized. This must, however, be taken with the understanding that new analytical procedures, considerations, and rigorous protocols are critical in order to better establish reproducibility and accuracy. With proper precautions and an understanding of appropriate limitations, electron microprobe analysis has the potential to reveal detailed and unique aspects of geologic processes, particularly in deciphering complex tectonic histories involving multiple events.

BACKGROUND

The recognition that radiogenic Pb would accumulate, over hundreds of m.y., in quantities that should be easily detectable with the electron microprobe, has encouraged several studies [dating back to at least 1968, see Bowles (1990)] to attempt “chemical,” or total-Pb geochronology on materials rich in Th and/or U (uraninite, thorite, monazite, etc.). Attempts to work with monazite have become increasingly common, due to the observation that common Pb abundances are generally small relative to radiogenic Pb (Parrish 1990), and that monazite, although an accessory mineral, is remarkably ubiquitous, especially in multiply deformed, medium- to high-grade metamorphic rocks. There are two basic approaches: (1) to measure many spots in a selected grain with sufficient compositional variation in domains of constant age to be able to construct a “pseudo-isochron,” from which an age can be obtained by regression [the so-called CHEMICAL Isochron METHOD (CHIME), pioneered by Suzuki and Adachi 1991]; or (2) to compute an age for a few analytical spots restricted to a single compositional domain (based on casting the age equation in terms of generated Pb from ^{232}Th , ^{235}U and ^{238}U), and after propagating uncertainties, accumulating enough points to resolve a meaningful age, pioneered by Montel et al. (1996). The CHIME technique is generally applied to large monazite grains (usually obtained from mineral separates) and is based on the assumption of sufficient compositional variability in domains of constant age. Many points are necessary to attain a reasonable “isochron.” However, the method has the potential advantage of substantial precision under the right circumstances (Suzuki and Adachi 1998; Cocherie and Albarede 2001), and this regression-based technique has the ability to work with minerals having substantial common Pb. Refinements include use of independent U-Pb and Th-Pb age estimates (Rhede et al. 1996). The single-point technique of Montel et al. (1996) has the advantage of application to exceptionally small monazite grains directly in thin section and is not limited by absence of compositional variability, actually lending itself to direct sampling of single compositional domains. Williams et al. (1999) and Williams and Jercinovic (2002) advocate using high-resolution X-ray maps to define domains to be analyzed independently, then sampling those domains until an appropriate statistical precision has been obtained.

The relative accessibility, ease, and versatility of microprobe analysis encourages exploration into new analytical territory, for example, attempts have been made to analyze not only monazite, but uraninite (Parslow et al. 1985; Bowles 1990; Cheong et al. 2002; Kempe 2003), xenotime and zircon (Suzuki and Adachi 1991; Asami et al. 2002), badelleyite (French et al. 2002), thorite, and huttonite (Lumpkin and Chakoumakos 1988; Förster et al. 2000) by EPMA for geochronology, with varying degrees of

success. Each mineral poses particular analytical challenges and the exact methodologies will continue to require refinement, the compensation being the potential benefits of broadly applicable, rapid, in-situ microanalysis.

RESULTS

Any attempt to evaluate analytical variables is fundamentally machine dependent. There are many physical variables involved in electron microprobe analysis that require knowledge not only of the general properties of a machine, but also of the highly specific nature and behavior of individual components of that machine. For example, no two X-ray detectors behave exactly the same, meaning that our observations of properties such as count rates from standards or estimated dead-times or noise levels require direct measurement from each detector. As such, no presentation of an analytical “cookbook” can be generally applied. The results presented below are representative of the hardware and software applied to the problem. In this case, we have used a Cameca SX50 electron microprobe running under Cameca’s SXRAYN50 software for data acquisition, including Cameca’s implementation of PAP matrix corrections in all cases. The instrument used has four wavelength-dispersive spectrometers, all with P10 flow-proportional counters. Two counters are kept at a pressure of approximately 1 bar, and the other two counters are run at approximately 3 bars total pressure. For the analysis of $\text{Y}\text{L}\gamma$, $\text{ThM}\alpha$, $\text{PbM}\alpha$, and $\text{UM}\beta$, we use TAP (low P), PET (low P), PET (high P), and PET (high P), respectively. As with all Cameca SX series instruments, the spectrometers have a characteristic 160 mm Rowland circle radius.

It is of critical importance to recognize that ionization efficiencies and X-ray escape probabilities are density (pressure) dependent, therefore, spectra and line intensities collected from low-pressure counters cannot be compared directly with similar acquisitions from high-pressure counters. The collection of $\text{PbM}\alpha$ X-rays in one type of counter will require a very different detector voltage (bias) and pulse-height analysis (PHA) baseline and window settings relative to other counters at a different pressure. Likewise, the comparison of spectra obtained from a Cameca SX electron microprobe will appear substantially different compared to spectra collected on a JEOL JXA electron microprobe which uses a 140 mm Rowland circle, leading to differences in spectral resolution and consequently differences in interference intensities. Similarly, the behavior of X-rays interacting with the detector gas will also differ with detector gas mixture and the presence or absence of exit windows. A Cameca counter will, unless otherwise modified, have argon-10% methane (P-10) flow proportional counters at a selectable pressure and beryllium exit windows. Detectors used in JEOL JXA instruments are generally supplied without exit windows, and have both low-pressure P-10 flow-proportional counters as well as sealed counters containing 10 to 60 torr partial pressure Xe with the balance being quench gas (Geller and Herrington 2002). The overall detector issue has become a significant point of debate relating to the electron microprobe analysis of monazite. Therefore, new investigations have recently been initiated to examine the relative effects, and detailed evaluation of these results will be forthcoming. Software is clearly of fundamental importance as well: this is where current measurements, dead-

time corrections, background subtraction, interference corrections, matrix corrections, and other procedures are implemented in the process of calculating the element concentration we see as the final "result." We make no attempt to directly explore these comparisons in detail in this paper, but strongly caution readers to consider all of the pertinent variables when attempting trace element analysis.

Beam effects and coating materials

Th-U-Pb geochronology by EPMA is essentially a trace-element technique, involving the precise, accurate analysis of Th, U, Pb, and Y, any or all of which may be present at levels considerably lower than 1000 ppm. Trace-element EPMA requires the use of exceptionally high beam current (typically hundreds of nA) coupled with long count times (10 min or more) to optimize counting statistics, while still maintaining a small beam size to maximize spatial resolution. At such high beam power density (100–1000 $\mu\text{W}/\text{cm}^2$, after Gunn et al. 1992), the large resistance of the target necessitates a highly conductive surface coating, and it is essential that the effects of these exceptional beam parameters be assessed with regard to both sample damage and charge effects.

Measured sample current reflects the proportion of current flowing to ground in conductive specimens. Changes in the measured sample current during the X-ray acquisition time reflect the disequilibrium buildup of charge within the specimen and/or changing electron emission characteristics. As space charge accumulates within the specimen, an effective surface potential will be generated that influences incoming beam electrons entering the specimen, and leads to dynamic shape distortion of the excitation and X-ray production volumes, and ultimately leads to unpredictable X-ray emission characteristics. Typically, for monazite trace element analysis with a nominal carbon coat thicknesses of 250 Å, (as determined by the interference-color method of Kerrick et al. 1973) at 200 nA and 15 kV (focused beam), the measured absorbed current drops significantly after a few minutes, in some instances partially recovering or even oscillating slightly with time (Fig. 1). This behavior implies that the electrical properties of the coat are insufficient, and suggests either lowering the applied current density by decreasing current or increasing beam diameter, or, alternatively, using a coating material of higher electrical (and thermal) conductivity. Increasing the beam diameter to approximately 10 μm appears to eliminate or minimize absorbed current instability (Fig. 1). If high spatial resolution is required, then metallic coatings should be explored. Although several materials are viable in this regard, possible interferences from the coating material, as well as possible effects such as oxidation during heating and interaction with relatively common hydroxylated monazite associates such as muscovite, biotite, amphibole, or florencite also must be considered. Although not all possibilities were directly evaluated, gold was chosen over other metallic coatings as it appears to meet the initial criteria, assuming that it can be evaporated onto the specimen at a thickness considerably less than that of carbon (to counter the high absorption of the M-series X-ray lines of interest) and still maintain continuity over the surface of a thin section.

A thin gold coat can be evaporated onto the specimen surface,

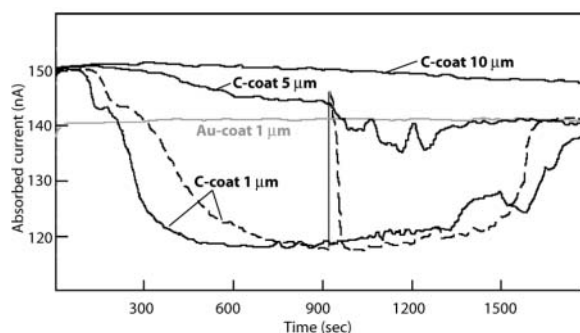


FIGURE 1. Absorbed current in monazite as a function of time and beam diameter. The carbon-coat thickness is about 250 Å, the gold coat is about 100 Å. The monazite is LGG246-5 from the Lower Gorge of the Grand Canyon. Test parameters: 15 kV, 200 nA, 3 s sampling period. Dashed line is a test run for 900 s, then interrupted (beam blanked) for 12 h, then resumed on the same spot.

which leads to a significant improvement in electrical performance (Fig. 1). Any high-vacuum thermal evaporation coater can be adapted for gold coating. The measured absorbed current remains relatively constant with a 200 nA focused beam on monazite for exposure times exceeding 30 minutes. Note that this result also implies that the current drop seen with a focused beam with carbon coating cannot be explained by simple contamination as both gold and carbon coats exhibit nearly equivalent carbon buildup at the point of beam impingement. Figure 1 also shows an experiment where beam exposure was interrupted after 900 seconds for a period of 12 hours, then resumed. This test shows that the sample returns rapidly to low absorbed current following re-exposure, implying that the behavior seen in the initial 900 seconds of exposure is not a simple thermal response. The expected drawbacks to using gold as a conductive coat include the relatively large mass absorption coefficients associated with heavy metals and potential interferences arising from the coat. Because gold has substantially lower electrical resistivity compared to carbon (2.4 $\mu\Omega\text{ cm}$ vs. 3500 $\mu\Omega\text{ cm}$ at 300 K), a relatively thin coat (<150 Å) can be applied, still obtaining an order of magnitude improvement in surface conductivity. The gold coat thickness for the thin section used in Figure 1 is estimated to be ca. 97 Å (by X-ray absorption measurements and using the fractional intensity loss calculation of Reed 1993). The predicted decreases in count rate relative to carbon for $\text{PbM}\alpha$, $\text{UM}\beta$, and $\text{ThM}\alpha$ are shown in Figure 2, indicating that a 97 Å gold coat produces a decrease in $\text{PbM}\alpha$ count rates (compared to a 250 Å carbon coat) of about 8%. However, although a thin gold coat can be highly conductive, the presence of surface relief (from polishing-hardness contrast), especially if abundant micas are present in the section, can cause loss of continuity of the coat and result in charging effects. In such cases, a thicker coat must be applied (as much as double), with the accompanying sacrifice in count rates. Alternatively, surface relief must be reduced. Clearly, excellent sample preparation and polishing techniques, which minimize surface relief in complex geologic samples is necessary to minimize these problems. A final polish with colloidal silica can improve the surface substantially (J. Pyle and F. Spear, personal communication). The high absorption characteristics of

metallic coatings such as gold also necessitate coating samples and standards at the same time, with care taken to ensure that geometric effects within the coater do not produce appreciable film thickness variations between the two.

Potential interferences from characteristic X-rays originating from the conductive coat are a major consideration when using evaporated metals. Monazite trace-element analysis requires the careful acquisition of counts using $PbM\alpha$, $UM\beta$, and $ThM\alpha$ (also $YL\gamma$, to monitor the intensity of $YL\gamma$, which interferes with $PbM\alpha$). Fortunately, the only significant interference relevant to these lines is the $AuM\gamma$ family, which occurs on the high-wavelength side of $PbM\beta$. A heavy gold coat can produce measurable interference between $AuM\gamma$ and $PbM\beta$, although this could be accounted for explicitly by interference correction if the $PbM\beta$ line were required. As samples and standards should have identical coating thicknesses, this effect should be minimal.

Compositional changes in monazite associated with electron beam exposure

Beam irradiation even at moderate doses (e.g. 10–20 nA, 2 μ m diameter) can result in thermally activated (or enhanced) effects such as dehydration of micas, decomposition of carbonates and phosphates, and alkali migration in targets such as feldspar or glass, even with an otherwise acceptable carbon coat (e.g., Walker and Howitt 1986; Gunn et al. 1992; Stormer et al. 1993; Spray and Rae 1995). Beam damage has been suggested to be responsible for charge-balance effects, resulting in wavelength shifts during analysis (Wallace and Carmichael 1992). Temperature rise in insulators under beam exposure is a significant factor in these processes. The manifestations of such “beam damage” should always be considered in EPMA, but certainly must be evaluated when a very large beam dose is proposed.

A portion of the energy transferred to the specimen by in-

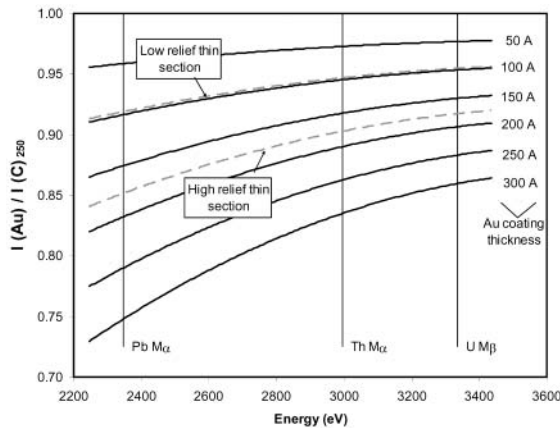


FIGURE 2. X-ray intensity as a function of gold-coat thickness (in angstroms). Gold-coat thickness is estimated from known carbon-coat thickness of ca. 250 Å, using the fractional intensity loss expression of Reed (1993). Curves for thin sections delineate approximate thickness where adequate coat continuity is consistently obtained. Conductive continuity is evaluated by observing beam shift across the section, and is considered adequate when no observable shift is noted over the entire section. Note that greater thickness is required in cases where surface relief is relatively high.

elastic scattering is expressed as heat (phonon excitation). The temperature increase expected in complex geologic samples is difficult to assess quantitatively because the behavior of the mineral being analyzed will be affected by surrounding materials. Although bulk thermal conductivity may provide an approximation for uncoated specimens, the true thermal behavior will be critically dependent on the surface conductive coat as well, and use of coating materials with high thermal conductivity should dramatically reduce heat damage. To better evaluate the analytical consequences, compositional changes were evaluated by measuring the major-element concentrations in monazite both before and after beam exposure, comparing carbon and gold coats.

Monazite with a nominally conductive carbon coat (250 Å), exposed to a focussed electron beam at 15 kV and 200 nA for 600 s, develops a bright spot at the irradiation point in high-contrast back-scattered electron (BSE) images (Fig. 3). This bright spot persists, even with repeated polishing. Although these spots are useful for precise post-acquisition beam location assessment, they also imply that the target has been compromised as a result of beam exposure. Because the BSE contrast is primarily a function of average atomic number, the bright spots suggest a compositional change (increase in average Z) during analysis.

One way to assess the magnitude of beam irradiation effects on the composition of monazite is to measure the major-element composition using moderate current densities, on a single spot, both before and after high current irradiation. This is illustrated by experiments on monazite in samples from the Lower Gorge of the Grand Canyon. The example monazite is in a thin section (LGG246-5) that initially was carbon coated, compositionally

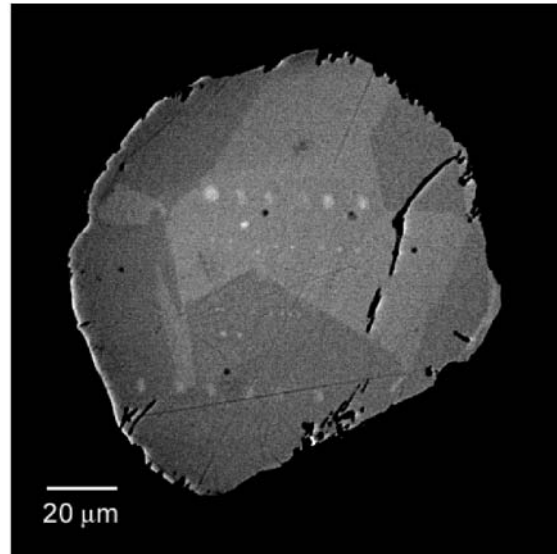


FIGURE 3. Back-scattered electron image of monazite LGG246-5m1, from the Lower Granite Gorge of the Grand Canyon. Note bright spots from high-current (200 nA, 15 kV, 30 min) beam exposure with a carbon coat: smaller ones are from focused beam, larger ones are from slightly defocused beam. No bright spots remain after high-current exposure with a gold coat. Sector zoning is apparent, contrast primarily follows Th content in this case. (See Fig. 10).

mapped, then detailed major-element analyses were performed (15 nA, 15 kV) in each compositional domain. After major-element analyses were obtained, the beam was set to 200 nA and focussed, then exposed to spots in the same domain for 30 min each. An exposure time of 30 mins was selected as typical trace-element acquisition times are usually 10 to 15 mins. Measured backgrounds would require a 20 to 30 min exposure, or, if backgrounds are acquired by WDS scanning (as we advocate here), exposure times can exceed 30 mins at high current. Once high-current exposure was completed, the beam was then returned to 15nA and re-focused, and major-element analyses were obtained from the easily identified spots. The results indicate a significant loss of P, with a complementary increase in other major elements due to high current exposure (Fig. 4). The compositional change corresponds to an increase in average atomic number of approximately 7%. It should be emphasized that if these bright spots are seen after quantitative analysis, then the sample has been compositionally compromised at these spots. This observation, along with the behavior of the absorbed current (above) during the 30 min exposure at 200 nA, encouraged exploration of other coating materials.

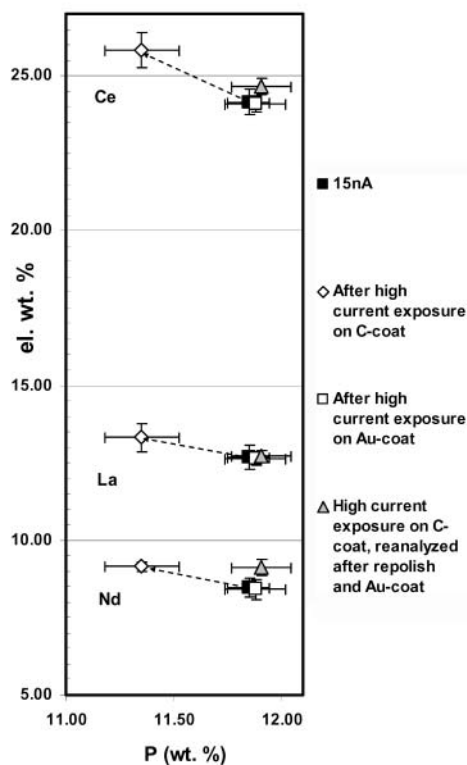


FIGURE 4. Compositional effects of high-current beam exposure (200 nA, 15 kV, focused beam for 30 min). Major-element analyses (15 nA, 15 kV, focused beam) of “bright spots” such as those in Figure 3 compared to similar analyses done after gold coating. Loss of P relative to REE is indicated. Although the bright spots persist to some extent after polishing, re-analysis after polishing and recoating with gold do not show appreciable compositional differences compared to 15 nA analyses (gray-filled triangles above). High-current exposure of gold-coated monazite does not produce any measurable effect in major-element analyses.

The results for the same high beam current (200 nA, 30 min) experiments after re-polishing the same thin section (LGG 246-5) and gold coating (high-vacuum thermal evaporation to approximately 100 Å), show a very stable absorbed current level (Fig. 1) and no visible “bright spots” in BSE imaging. The beam location could, however, be seen in BSE as dark spots, due to carbon buildup on the surface of the monazite during high current exposure. Interestingly, the bright spots from the previous analyses were still visible, although somewhat less evident after repolishing and gold-coating. Major-element analysis of the monazite on the gold-coat exposure spots shows little compositional change relative to the monazite not exposed to high current (Fig. 4). Re-analysis of the bright spots, which still persist from 200 nA exposure with carbon coating, still show P depletion.

Most relevant to geochronologic applications are the relative concentrations of Pb, Th, and U. In the above example, the Pb concentration is not a reliably accessible measurement at 15nA, but the U and Th values can be addressed to some degree. Analysis of the high current spots in the carbon coat test show that both U and Th concentrations increase in the spots during analysis. A change in U/Th is difficult to evaluate (Fig. 5), although there is some suggestion that U and Th do not behave identically during this process, leaving a slight excess in U relative to Th. With a gold coat, concentrations on and off of high-current exposed spots are statistically indistinguishable (Fig. 5).

BACKGROUNDS AND INTERFERENCES

Background shape and general compositional dependence

The consequences of inaccurate background subtraction can potentially be quite dramatic in EPMA applications in geochronology, especially as Pb, Th, and U concentrations approach the true trace-element range. The Pb concentration, in particular, will typically govern the precision of the age estimation. However, Th or U may not also exist in exceptionally low concentrations, where small errors in peak or background measurement can result in large errors when propagated through the age calculation. As the P/B ratio approaches 1, the analysis becomes more tenuous, and the correct contribution of the

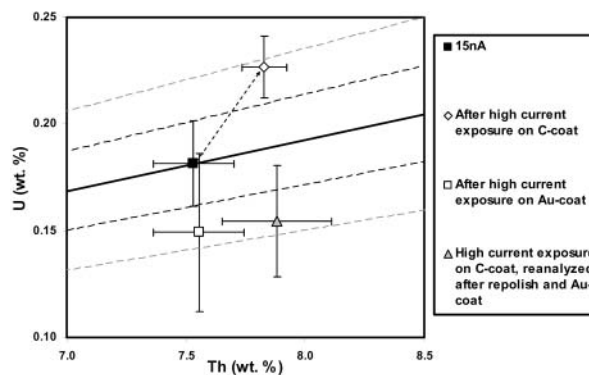


FIGURE 5. Uranium and Th contents (15 nA, 15 kV, focused beam, 90 s counts) in monazite before and after high-current exposure. Curves indicate constant U/Th with $\pm 1\sigma$ (heavy dash) and 2σ (light dash) precision.

background becomes more critical.

Most EPMA applications estimate background intensities by measuring intensity at appropriate, predetermined wavelengths above and below the peak of interest, and calculating the intensity under the peak via linear interpolation. This procedure assumes that any subtle curvature in the background will be relatively inconsequential, an assumption that is generally valid for short wavelength distances relative to peak height, especially for major-element analysis. This assumption will be challenged for low P/B ratios. Theoretical background intensity has been addressed by Kramers (1923) and subsequently refined (e.g., Ware and Reed 1973; Lifshin et al. 1975; Fiori et al. 1976; Small et al. 1987; Reed 1993; Geisler and Schleicher 2000). Continuum emission, expressed as photons/unit energy interval, has a natural curvature, with intensity increasing toward lower energy. As noted by Lifshin et al. (1975), Kramers' constant is, itself, a function of average atomic number, beam voltage, and energy interval, factors that result in substantial curvature in actual emission spectra. The influence of composition is substantial (Goldstein et al. 2003; Donovan and Tingle 1996). Emission spectra are, in fact, further complicated by absorption edges for constituent major elements and other factors relating to the detection system. The background intensity and curvature are strongly influenced by spectrometer efficiency, itself a complex function of the proportion of the X-ray emission cone entering the detector that is intercepted by the analyzing monochromator at different wavelengths, complicated at low diffraction angle by the effects of specular reflection (Fialin et al. 1999). In general, X-ray emission modeling predicts increasing background intensity toward lower energy (longer wavelength), whereas spectrometer efficiency considerations produce increasing intensity toward higher energy (shorter wavelength). X-ray intensity is also a function of the counter gas quantum efficiency dependence on photon wavelength, and will also vary with absorption in the sample and by windows in the detection system. All of the above factors make the exact shape of the background highly complex, and hardware factors such as counter gas composition and pressure, pulse-height discriminator window width, detector bias, dimensions of the monochromator, the presence or absence (and width) of collimating slits, and Rowland circle radius necessitate direct measurements made on each spectrometer. Even if potential interferences are predictable, accurate trace-element analysis requires direct measurements and assessment of background curvature and edge features appropriate to the peaks of interest.

With the above considerations in mind, along with the observation that P/B ratios are commonly very low in trace-element analysis (routinely 1.1 to 1.5 for $PbM\alpha$ in monazite), it is not surprising that background subtraction using 2-point interpolation can produce inconsistent or inaccurate trace-element results in microprobe geochronology. Accounting for background shape effects can be approached statistically (Fialin et al. 1999) or through subsequent refinements of emission modeling (Ware and Reed 1973; Small et al. 1987; Geisler and Schleicher 2000). Alternatively, wavelength scanning allows the direct estimation of the shape of the background as well as the assessment of the influence of characteristic lines. Background segments can be selected from such spectra and used for calculation of background

intensity under the peaks of interest using appropriate curve-fitting models (polynomial, exponential, or linear).¹

Wavelength scanning, filtering, and deconvolution

Accurate evaluation of peak interferences and background selection involves comprehensive spectral analysis. Detailed wavelength scanning results in a direct measure of spectral structure, including background intensity, shape, and the character of absorption edges. Appropriate background intensities can be extracted directly from spectral data if peaks and absorption edges can be identified and filtered. In addition, peak interferences (and interference corrections) can be evaluated correctly if the peaks involved can be deconvoluted directly from acquired spectra.

To evaluate wavelength scan data properly, the signal/noise ratio must be high enough to reveal the details of interest. Because noise arises from both counting statistics as well as a variety of electronic-measurement sources [e.g., shot noise, $1/f$ or "pink noise," Johnson noise; see Horowitz and Hill (1989)], noise reduction becomes critical where peak intensities are very low relative to the surrounding background spectrum.

The objective of a low-pass digital filter is to eliminate the high-frequency noise in a time-uniform signal, and must allow an accurate representation of overall intensity variation as a function of wavelength, as mentioned above, and lower-frequency features (peaks, edges). To avoid the degradation of amplitude and increase in peak width associated with moving averages, a smoothing polynomial, or Savitsky-Golay, digital filter is suitable (Savitsky and Golay 1964; Press et al. 2002). This approach implements a polynomial expression for a moving data window of constant width, and is particularly straightforward and accurate in the case of step scanning as the data points are equally spaced in time. As long as the proper filter size (window width) and fitting-polynomial order are chosen, resolution and/or peak amplitude can be maintained. Scan parameters and selected filter attributes will depend, in part, on the spectral features of interest. In the case of background selection, the exact representation of peaks is less important than separating peaks from background regions in the spectrum (Fig. 6). In the case of deconvoluting interfering peaks or evaluating precise peak structure (e.g., asymmetric broadening due to non-diagram lines), scan and fitting parameters should obviously favor accurate peak representation (Fig. 7).

Wavelength scanning has the obvious benefit of revealing even minor concentrations of unexpected elements that will affect background measurements if not accounted for. These peaks can then be excluded from background intensity estimates. If

¹ We have developed macro programs (tasks) for the Cameca SX50 to acquire step scans and calculate dead-time corrected intensities. The scans can be adjusted to any wavelength step size, count time, and overall scan length. Scan data is written to an ASCII text file and can be imported into spreadsheets or data-analysis programs for display and evaluation. We have also developed a program that will import the scan data, implement low-pass noise filtering (Savitsky-Golay), allow selection of background regions, fit curves based on several regression models, and calculate background intensities at peak positions. These are available from the authors.

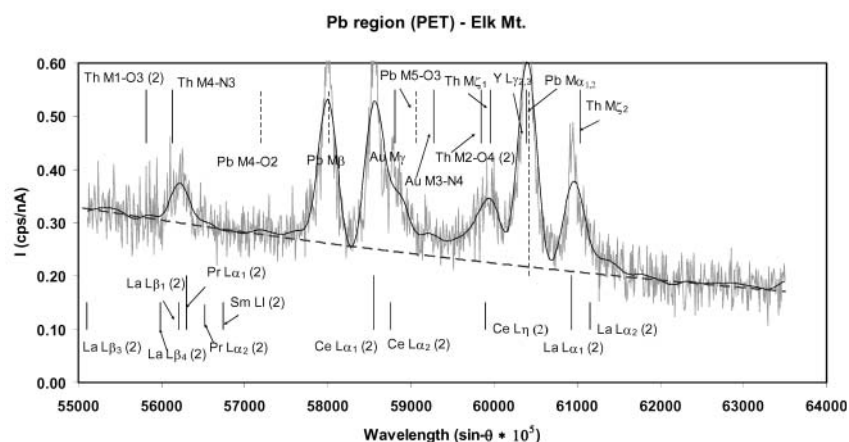


FIGURE 6. Wavelength scan from Elk Mt. monazite, Pb region on PET, differential PHA, P-10 counter gas at pressure ca. 2 bar. The scan was run with 0.00008-sin θ steps, 1.5 s/step at 200 nA and 15 kV (focused beam) on a 160 mm radius Rowland circle. Smoothing is done using a Savitsky-Golay digital filter optimized for background smoothing. The relatively wide window for the digital filter produces a reduction of peak height but no broadening, maintaining overall energy resolution and eliminating nearly all noise. The heavy gray curve is the calculated exponential best-fit for selected background regions (see Fig. 8a).

wavelength scans are acquired with sufficient resolution, precise peak shapes also can be used to evaluate peak overlaps. Once noise is effectively filtered, deconvolution routines can be implemented. Deconvolution requires knowledge of appropriate peak profiles as well as likely apparent broadening mechanisms such as the appearance and intensity of non-diagram lines and instrumental effects. Emission spectra are inherently Lorentzian (Cauchy distribution; Hölzer et al. 1977). Accurate deconvolution of WDS overlaps in measured spectra, however, requires that the natural emission profile be convoluted with Gaussian instrumental effects such as Doppler broadening and X-ray optical effects to obtain accurate peak shapes, best described by the Voigt function (Armstrong 1967; Ida et al. 2000; Rémond et al. 2002). This function can be approximated via the weighted sum of Gaussian and Lorentzian functions (pseudo-Voigt function), or the function can be solved analytically (true Voigt function). In this paper, we have used commercial software² for numerical peak deconvolution that utilizes a closed-form solution to calculate the Voigt function for defining peak profiles. In the applications of wavelength scanning below, we will illustrate the analytical effects of errors in background determination on EPMA geochronology, and attempt to extract peak overlap parameters affecting the measurement of Y, Th, Pb, and U directly from measured spectra. Scanning provides a means of evaluating details of spectral structure impacting both background and peak intensity measurements.

Background shape

The effect of background shape on monazite geochronology is illustrated by spectra acquired from monazite from Elk Mt., NM. Thorium, U, and Pb were measured using PET monochrometers and P-10 counter gas (ThM α on low pressure, ca. 1 bar counter, UM β and PbM α on high pressure, ca. 2–3 bar counters). Because Th is typically present at the weight percent level, it is somewhat less sensitive to errors in background estimation in many (but certainly not all) cases. Figure 8 illustrates the essential concept of background estimation on the Pb spectrum, showing the difference between 2 point interpolation and curve fitting for the estimation of background for PbM α . The calculated background

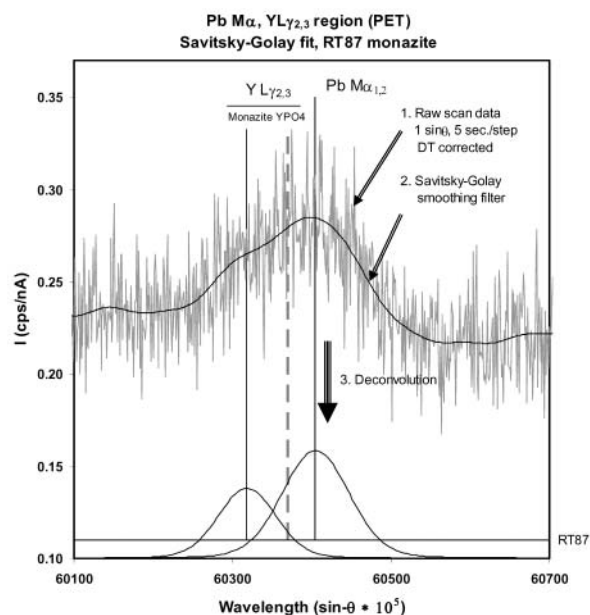


FIGURE 7. Procedure for deconvolution. A detailed wavelength scan is acquired (in this case 0.00001-sin θ steps, 6 s/step, 200 nA, 15 kV, focused beam), followed by noise reduction via Savitsky-Golay filter, background subtraction, then deconvolution using Voigt profiles.

values, concentrations, and age results are given in Table 1. For comparison, the results are also shown for backgrounds obtained by linear interpolation, using two different low-wavelength offsets for Pb (Fig. 8, Table 1). As Pb typically has the lowest concentration of the three elements, even a relatively minor shift in background intensity can produce a dramatic effect on the k-ratio and resulting concentration and age. As this example indicates, the choice of background model on PbM α alone results in a discrepancy of nearly 100 ppm and 17 m.y., and the effects can be much greater if the selected background offsets are inappropriate. A second example of younger monazite from Norway (Table 1) illustrates that this sensitivity can be significantly enhanced at lower Pb concentration in some monazite, in this case resulting in an age error of 35 m.y. Although the effects of using linear interpolation for background estimation for U and Th as well as

² PeakFit (Systat Software, Inc.)

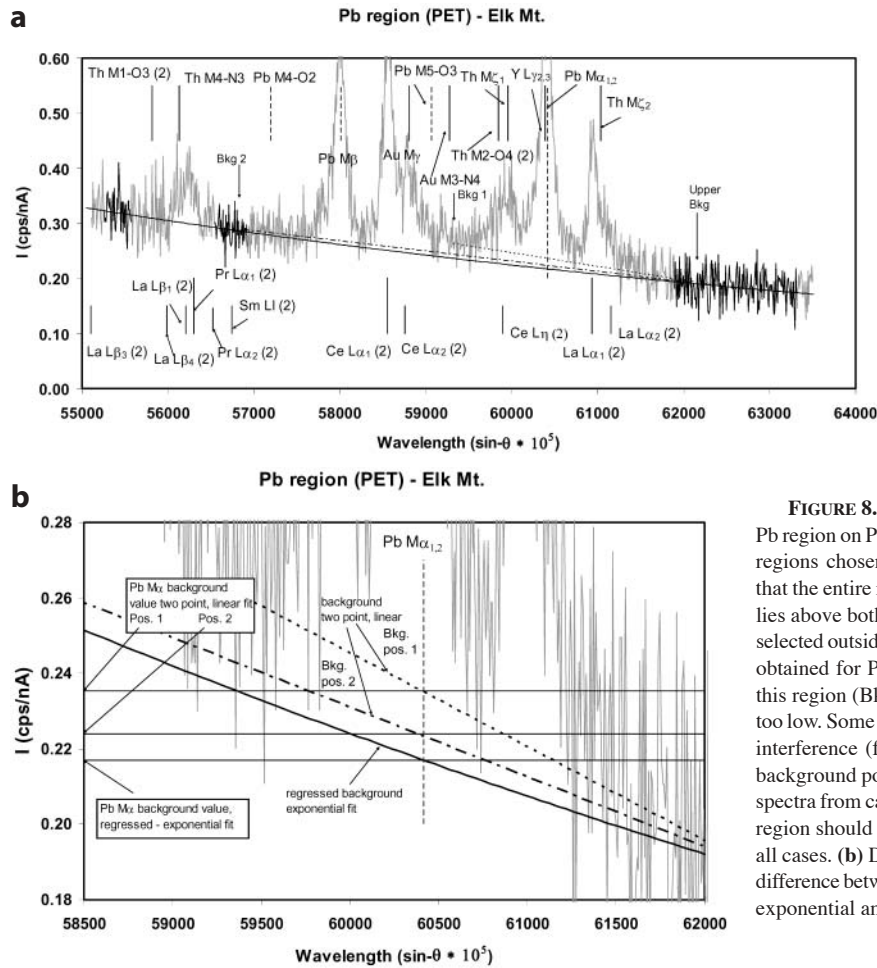


FIGURE 8. Raw wavelength scan of Elk Mt. monazite, Pb region on PET. (a) Highlighted regions of the scan show regions chosen for inclusion in background fitting. Note that the entire region between $ThM\zeta_1$ and $CeLa\alpha$ (2nd order) lies above both background curves when backgrounds are selected outside of this region. If two point backgrounds are obtained for $PbM\alpha$ using the low-wavelength position in this region (Bkg 1), the resulting Pb concentration will be too low. Some of the elevation of this region is due to $AuM\gamma$ interference (from the conductive coat), but the selected background position appears free of interferences. Similar spectra from carbon coated monazites also suggest that this region should be avoided for background measurement in all cases. (b) Detailed view of the $PbM\alpha$ region in 8a. The difference between linear (lower background position 2) and exponential amounts to about 100 ppm in this example.

TABLE 1. Concentrations of Y, Th, Pb, and U, and calculated ages, for Elk Mt., NM and RT87-17 (Romsdalen Traverse, Norway) monazites using backgrounds obtained by exponential fitting of background regions compared to 2-point interpolation

| | | | Concentration (ppm) | | | | Age (Ma) | N |
|---------|--------|--------|---------------------|--------|------|------|----------|----|
| | | | Y | Th | Pb | U | | |
| Elk Mt. | fitted | Ave | 6494 | 119215 | 8453 | 3586 | 1395.2 | 15 |
| | bkg. | SStd | 105 | 2172 | 141 | 218 | 15.3 | |
| | | StdErr | 27 | 561 | 36 | 56 | 4 | |
| Elk Mt. | linear | Ave | 6462 | 119184 | 8052 | 3560 | 1333.0 | 15 |
| | bkg. | SStd | 120 | 2218 | 174 | 228 | 16.8 | |
| | Pos. 1 | StdErr | 31 | 573 | 45 | 59 | 4.3 | |
| Elk Mt. | linear | Ave | 6462 | 119184 | 8279 | 3560 | 1368.9 | 15 |
| | bkg. | SStd | 120 | 2218 | 136 | 228 | 15.2 | |
| | Pos. 2 | StdErr | 31 | 573 | 35 | 59 | 3.9 | |
| RT87-17 | fitted | Ave | 19196 | 48043 | 1094 | 3984 | 400.2 | 5 |
| | bkg. | SStd | 3518 | 3043 | 119 | 1343 | 8 | |
| | | StdErr | 1573 | 1361 | 53 | 601 | 3.6 | |
| RT87-17 | linear | Ave | 19194 | 48007 | 996 | 3958 | 365.4 | 5 |
| | bkg. | SStd | 3519 | 3039 | 123 | 1340 | 10.1 | |
| | | StdErr | 1574 | 1359 | 55 | 599 | 4.5 | |

Notes: The IDTIMS $^{207}Pb/^{206}Pb$ age for the Elk Mt. monazite is 1394 ± 1 Ma (J. Baldwin and S. Bowring, unpublished data). The IDTIMS age for RT87-17 is 394 ± 1 Ma (Tucker et al. 1990).

Pb can partially cancel in the age calculation (counts are truncated for all three elements), the low Pb concentration typically will result in the largest error, outweighing the U and Th underestimation and resulting in an underestimation of the age.

Compositional dependence

The average atomic number of monazite is essentially controlled by the proportions of actinides, in nearly all cases Th being the most significant, relative to the rare-earth elements (REE) and Y. Therefore, a relatively high background level at any selected photon energy is expected in higher Th relative to lower Th monazite. This relationship is illustrated in a comparison of spectra from high-Th monazite and synthetic, Pb-free YPO_4 (Fig. 9). Importantly, measured background intensities can vary considerably for $PbM\alpha$ in monazite domains showing a range of Th concentrations (Fig. 10). Therefore, it is critical to measure background in each compositional domain to prevent potentially serious analytical error. As noted above, the analysis of minor concentrations requires exceptionally careful background acquisition. Two-point acquisition is inaccurate and, even if reasonable results could be obtained by this method, the existence of possible background interferences also requires explicit knowledge

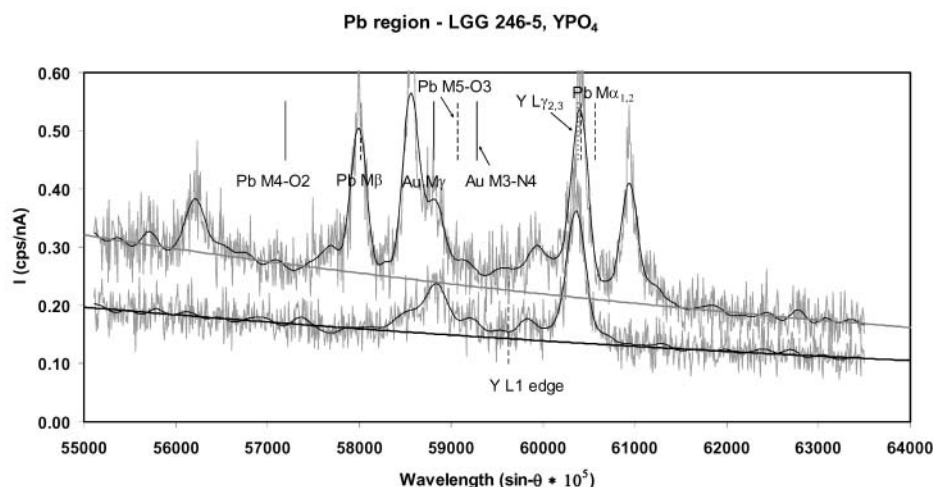


FIGURE 9. Wavelength scans (and Savitsky-Golay smoothing) of the $PbM\alpha$ region of YPO_4 (synthetic) and natural monazite (LGG246-5m1-Lower Granite Gorge of the Grand Canyon). Note generally higher scan intensity of higher average atomic number material (monazite) compared to YPO_4 . Scans were done using 200 nA, 15 kV, focused beam.

of spectral details at essentially every point where backgrounds are acquired. Because background intensity is a function of composition, background acquisition must conform to compositionally distinct domains. Mapping (Y, Th, U) of grains prior to background acquisition and analysis is clearly necessary in order to define compositional domains. Selected REE or other geochemically important elements also may be mapped, but for the purpose of background acquisition, the distributions of Y, Th, and U are generally sufficient to guide analytical strategy.

The effect of using a background intensity that is not constrained by the appropriate composition is illustrated in the following example from the Black Hills of South Dakota. Monazite from the Black Hills exhibits a large range of Th/REE (Table 2). High-magnification elemental mapping reveals high-Th cores and lower-Th rims in EG56, that yield analyses of 9.7 and 3.6 wt% Th respectively. Scanned backgrounds for this sample were obtained for monazite in the high- and low-Th domains (Table 2), and quantitative trace-element analysis yields an age of 1755 ± 6 Ma for the core and 1699 ± 19 Ma for the rim (Table 3). Note that, although there is no direct verification that the U, Th, and Pb concentrations are correct in these analyses, the ages of 1750–1760 Ma (Black Hills Orogeny) and ca. 1700 Ma (Harney Peak Granite) correlate favorably with isotopic geochronology in the Black Hills (Dahl et al. 2005). If the compositions for core and rim are attained, switching background values (that is, analyses are run in the high-Th core domain using backgrounds acquired from the low-Th rim domain, and vice-versa) both the concentrations and calculated age results are significantly different. The background difference for $PbM\alpha$ in Table 2 corresponds to approximately 60 ppm Pb, translating to +10 m.y. for the core, or -30 m.y. for the rim. In this case, the shift in apparent U concentration when backgrounds are switched ultimately results in a shift toward an apparently younger core and older rim. Overall, the calculated core age differs by 32 m.y. and the rim age differs by 70 m.y. depending on the background utilized, emphasizing the necessity of using background intensities representative of the composition of the domain being measured. Even monazite grains smaller than a few tens of micrometers across must be mapped in order to avoid improper background application and to ensure that analysis points do not overlap compositional

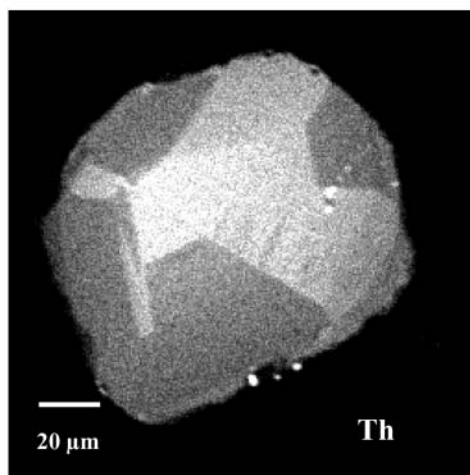


FIGURE 10. $ThM\alpha$ X-ray map of monazite LGG246-5m1 illustrating sector zoning defined by substantial Th differences. Higher-Th areas are brighter in the image. The high-Th core contains 7–8 wt% Th and the lower thorium domains contain 3–4 wt% Th.

boundaries (with resulting increase in analytical scatter from inhomogeneities in the excitation volume).

To summarize background effects, consider a second example using monazite from the Lower Gorge of the Grand Canyon (sample LGG 246-5, grain m1). Mapping of single monazite grains in a thin section from this sample reveals that all grains are compositionally zoned, and locally sector zoned (Fig. 10). Strong sector zoning of Th offers the opportunity to test the relationship between composition, background, and estimated age because the age should not vary from sector to sector. Acquisition of backgrounds (regressed from wavelength scans) from each compositional domain (Fig. 11) results in age estimations within each domain that are statistically indistinguishable at 1678 Ma (Fig. 12). However, if inappropriate backgrounds are used, that is, if background was acquired only from the high-Th domain and used in the low-Th domain, or if backgrounds were only acquired in the low-Th domain and applied to the high-Th domain as well, then the concentrations of Y, Th, Pb, and U shift, resulting in different calculated sector ages (1685 ± 13 Ma in the

TABLE 2. Representative analyses and background intensities for PbMa from distinct compositional domains in monazite grains from the Black Hills

| | Leg 8 wt% | prec. | Leg 8 wt% | prec. | Leg 8 wt% | prec. | EG 56 wt% | prec. | EG 56 wt% | prec. |
|--------------|--------------|-------|--------------|-------|--------------|-------|--------------|-------|--------------|-------|
| P | 12.96 | 0.12 | 12.45 | 0.12 | 11.83 | 0.11 | 11.86 | 0.11 | 13.11 | 0.12 |
| Ca | 0.06 | 0.01 | 0.84 | 0.02 | 1.49 | 0.03 | 0.51 | 0.02 | 0.64 | 0.02 |
| Th | 0.32 | 0.06 | 7.18 | 0.15 | 14.77 | 0.20 | 10.21 | 0.17 | 4.04 | 0.12 |
| Y | 0.77 | 0.09 | 0.89 | 0.09 | 0.70 | 0.09 | 0.21 | 0.07 | 0.58 | 0.08 |
| La | 14.04 | 0.36 | 14.49 | 0.37 | 10.35 | 0.30 | 15.20 | 0.38 | 13.77 | 0.36 |
| Ce | 26.29 | 0.45 | 24.95 | 0.44 | 20.40 | 0.38 | 23.68 | 0.43 | 27.26 | 0.46 |
| Nd | 10.53 | 0.26 | 6.24 | 0.20 | 7.42 | 0.21 | 6.28 | 0.20 | 8.16 | 0.23 |
| Pr | 2.64 | 0.21 | 2.11 | 0.20 | 1.98 | 0.20 | 2.07 | 0.20 | 2.27 | 0.20 |
| Sm | 1.94 | 0.20 | 0.54 | 0.18 | 0.93 | 0.18 | 0.59 | 0.17 | 1.32 | 0.19 |
| Gd | 1.67 | 0.47 | 1.23 | 0.46 | 1.04 | 0.46 | 0.00 | 0.00 | 0.00 | 0.00 |
| Bkg (cps/nA) | 0.207 | | 0.217 | | 0.223 | | 0.212 | | 0.218 | |

Note: prec. = $1-\sigma$ precision based on count statistics (in wt%).

high-Th domain using low-Th backgrounds, or 1666 ± 8 Ma in the low-Th domain if high-Th backgrounds are used (Fig. 12). Further inaccuracies would result if linear interpolation is used, giving 1653 ± 12 Ma and 1630 ± 8 Ma for high- and low-Th domains even if backgrounds are obtained and applied in like domains. The low-Th domain would yield 1633 ± 8 Ma if the 2-point backgrounds from the high-Th domain were used. 50 m.y. discrepancies can result from improper background application alone. These results emphasize the significance of mapping, followed by detailed background acquisition with appropriate, compositionally constrained, application during analysis.

Interferences and absorption edges

Many interferences involving characteristic X-ray lines relevant to general monazite analysis are well known, both with regard to major-element analyses and the geochronologically applicable trace elements [see, for example, Pyle et al. (2002); Sherrer et al. (2000)]. Analysts must be cautioned, however, in the utilization of tabulated X-ray data because properties such as relative line intensity and precise wavelength position can be misleading, especially when extrapolated to measurements in complex materials. Actual interference intensities and the details of peak structures are best evaluated by direct measurements whenever possible. Factors such as counter gas, precise crystal d -spacing, and spectrometer dimensions (Rowland circle radius), and peak positional shifts will affect the appearance and severity of such interferences. First-order interferences are certainly the most problematic, but higher-order lines can still result in spectral features even with the application of highly restrictive PHA windows. In some cases, escape peak interference may be significant in the energy window even if the higher-order characteristic peak is principally eliminated (Pyle et al. 2002). Corrections for peak interference typically involve estimation of a correction factor based on the apparent amount of the element of interest in a substance that contains the interfering element and none of the element of interest, by application of "interference standards," or by modeling of spectra (Amlı and Griffen 1975; Gilfrich et al. 1978; Roeder 1985; Donovan et al. 1993; Sherrer et al. 2000; Pyle et al. 2002). If correction is to be done by application of a factor (CF), the usual implementation is

$$\text{corrected}_{x,\text{unk}} = \text{measured}_{x,\text{unk}} - \text{CF} \cdot \text{measured}_{y,\text{unk}} \quad (\text{Pyle et al. 2002})$$

(1)

TABLE 3. Concentrations (in ppm) of Y, Th, Pb, and U, and calculated EPMA ages for Monazite EG56m9 from the Black Hills, SD

| | | Concentration (ppm) | | | | Age (Ma) | N |
|---------------------|--------|---------------------|-------|------|------|----------|---|
| | | Y | Th | Pb | U | | |
| Core high Th bkg | Ave | 8329 | 97462 | 8607 | 2230 | 1754.8 | 6 |
| | SStd | 335 | 6538 | 536 | 111 | 7.5 | |
| | StdErr | 137 | 2669 | 219 | 45 | 3.1 | |
| rim low Th bkg | Ave | 4862 | 35935 | 3476 | 2240 | 1698.7 | 7 |
| | SStd | 404 | 1918 | 177 | 109 | 25.5 | |
| | StdErr | 153 | 725 | 67 | 41 | 9.6 | |
| Core low Th bkg | Ave | 8201 | 97638 | 8668 | 2957 | 1722.9 | 6 |
| | SStd | 332 | 6539 | 531 | 111 | 6.3 | |
| | StdErr | 136 | 2670 | 217 | 45 | 2.6 | |
| rim high Th bkg | Ave | 4982 | 35770 | 3418 | 1559 | 1771.8 | 7 |
| | SStd | 403 | 1904 | 179 | 111 | 26.6 | |
| | StdErr | 152 | 720 | 68 | 42 | 10.1 | |

Note: Backgrounds obtained separately for core and rim and applied to core and rim trace analyses, then background intensities were swapped, applying high Th backgrounds to the rim analyses, and low Th backgrounds to the core analyses.

where x is the wt% (usually applied as wt% oxide) of the element of interest and y is the wt% of the interfering element. More rigorously, correction factors should be applied at the K -ratio level (see Pyle et al. 2005, this volume).

Interference corrections cannot be linearly applied directly from measurements on high-concentration standards due to matrix effects, peak-shape considerations, and possible wavelength shifts (Roeder 1985; Donovan et al. 1993). Peak positions may differ significantly from tabulated values or from standard to unknown, for example, a line such as $YL\gamma_3$ ($L1-N3$) will be more susceptible to compositionally related wavelength shifts, compared to Pb, Th, or $UM\alpha$ or $M\beta$ lines, as the $YL\gamma_3$ (in Y^{3+}) de-excitation transition involves the outermost, filled shell ($N3$ [$4p^{3/2}$]).

Relevant interferences may be fundamentally complicated, for example, extracting the true Pb concentration by measuring the $PbM\alpha$ line requires subtraction of $YL\gamma_{2,3}$, typically estimated based on the Y concentration attained by measurement of the $YL\gamma$ line on TAP. $YL\gamma$, however, is overlapped by Nd (the 3rd order $NdL\beta_{1,4}$ line), also a major component of most monazite (Fig. 13). The Nd interference on $YL\gamma$ can be effectively eliminated by careful differential analysis, but PHA behavior should be directly assessed and periodically monitored.

In both monazite and xenotime, measurement of the $PbL\alpha$ line (implying that at least 20 kV accelerating potential is used) should be avoided due to the first-order interference of $AsK\alpha$,

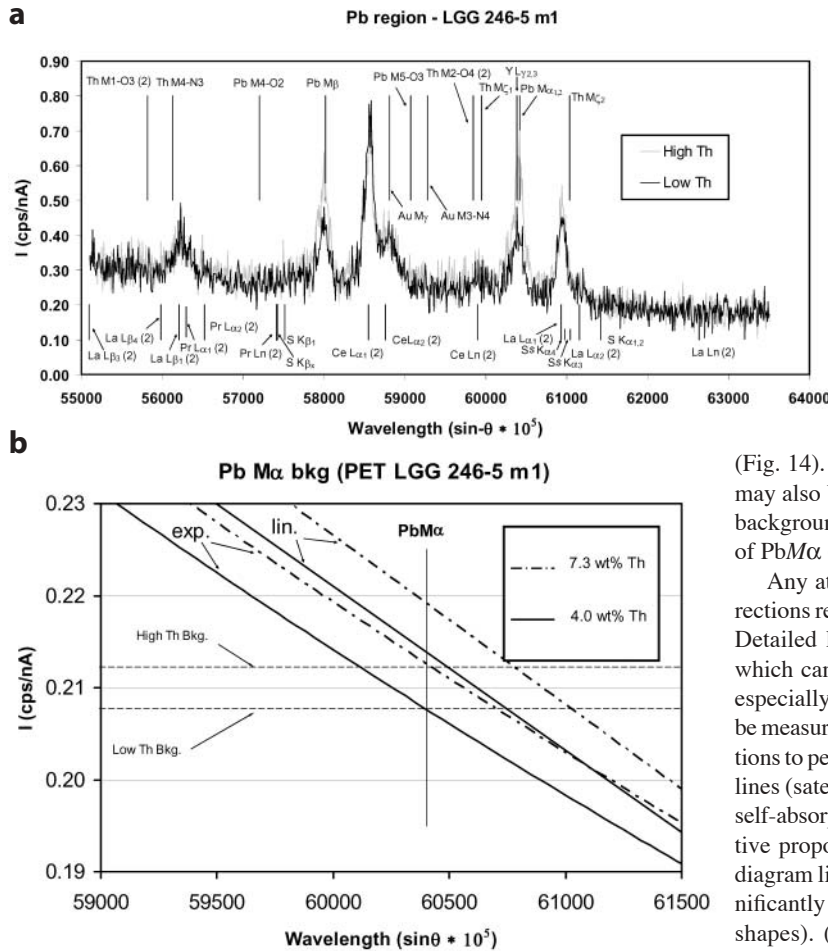


FIGURE 11. (a) Wavelength scans (PbM region on PET) of high- and low-Th domains in LGG246-5m1 (see Fig. 10). Note generally higher X-ray intensities throughout the spectrum for the higher-Th domain compare to a lower-Th domain. (b) Illustration of background levels for PbM α in high- and low-Th domains, using exponential fitting and linear, 2-pt. interpolation.

as As is a diadochic with P in both minerals. Although As is typically not measured in monazite, one should be wary of the arsenide (and vanadate) substitution: Gasparite, (REE)AsO₄, and chernovite (YAsO₄) form isomorphous substitutional solid solutions with monazite and xenotime, respectively. Although even a few tenths of a wt% As would clearly be very problematic, some monazite can contain significant substitution of As for P

(Fig. 14). Limited substitution of Si, V, Ca, S, and Bi may also be expected. Sulfur can particularly hamper background estimation on the high-wavelength side of PbM α (Fig. 15).

Any attempt to generate reliable interference corrections relies on several important considerations: (1) Detailed knowledge of electron transition energies, which can be complicated in heavy atoms (actinides especially). Positions and relative line intensities must be measured. (2) Estimation of lineshape and complications to peak structure from such things as non-diagram lines (satellite; Coster-Kronig transitions), differential self-absorption effects (in some cases affecting the relative proportion of satellite intensity compared to the diagram line) and strong absorption edges that can significantly affect both apparent peak and background shapes). (3) Possible wavelength shifts of diagram lines due to significant compositional differences, particularly when considering interference standards.

Interference intensity estimation can be based on the simple relationships (Bolz and Tuve 1976; Roeder 1985):

$$X = \frac{\lambda_d - \lambda_i}{W/2} \quad (2)$$

for estimating the amount of spectral overlap; and

$$F = e^{-(X^2/2)} \quad (3)$$

the Gaussian function for estimating the fraction of counts, where X is the magnitude of overlap, λ_d is the wavelength position of the desired peak, λ_i is the wavelength position of interfering peak, W is the peak width (measured at half height, assuming both peaks are similar), and F is the resulting fraction of counts from the interfering peak at the position to be measured. A correction factor can then be obtained by multiplying F by the relative peak intensity (percentage of the peak heights of interfering to measured lines for the interfering element), which can then be subtracted from the total intensity at the position of the peak of interest.

With L and M lines of heavy elements, however, significant complexities are introduced that can limit this approach. In particular, the assumption of Gaussian lineshape has been demonstrated to be inaccurate (Rémond et al. 2002). Peak-shape considerations must include the overall spectral contribution of

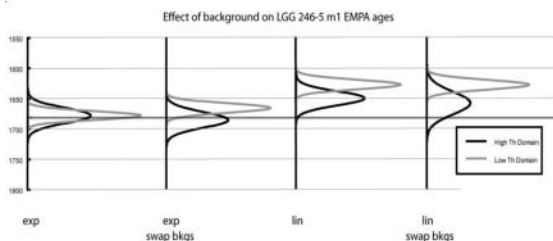


FIGURE 12. Summary of age results for high- and low-Th domains in sector-zoned LGG246-5m1. Curves are normal distributions representing the average and 2 \times standard error of the population of analyses within a domain. Exponential background fitting produces consistent ages between domains. Use of backgrounds from the “wrong” domains (swapped backgrounds) produces divergence in the sector ages. Use of linear backgrounds lowers the apparent age. The heavy gray line at 1681 Ma represents the IDTIMS age of monazite from this sample (K. Davidek and S. Bowring, personal communication).

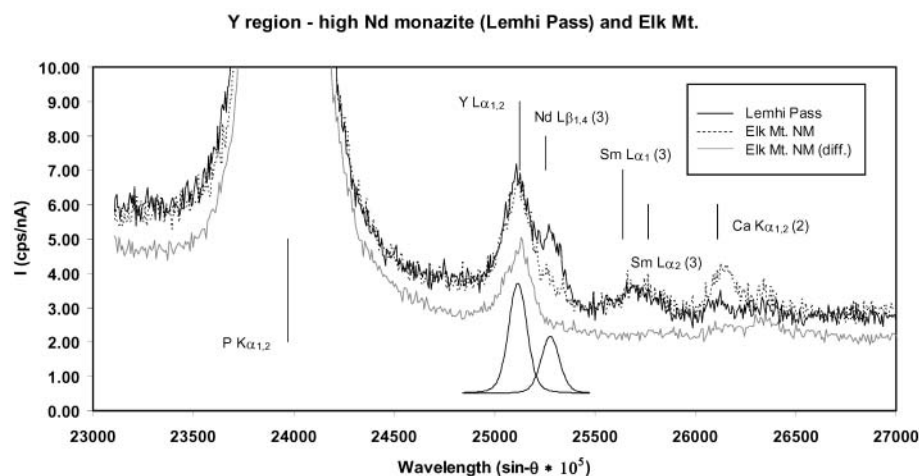


FIGURE 13. Wavelength scans of the $YL\alpha$ region (TAP) from high-Nd monazite from the Lemhi Pass Thorium district, Idaho (29–30 wt% Nd, 0.5 wt% Y), compared to Elk Mt. monazite (9.1 wt% Nd, 0.7 wt% Y). Note the $YL\alpha$ peak shape difference from integral to differential (diff.) PHA modes in the Elk Mt. monazite, illustrating the reduction of the of the $NdL\beta_{1,4}$ (3rd order) line. The deconvoluted peak profiles (background subtracted) for the Lemhi Pass monazite are shown at the bottom of the figure.

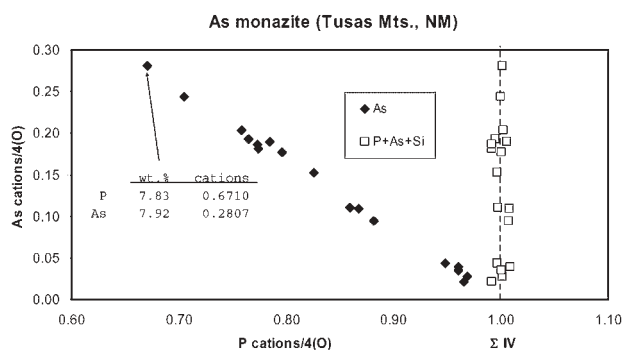


FIGURE 14. Arsenic/phosphorous cation proportions (normalized to 4 O atoms) in monazite from the Tusas Mountains, New Mexico. The total tetrahedral cation proportion (ΣIV) is constant at 1 per 4 O, indicating substitution of As for P in the tetrahedral site.

lower-energy transitions modifying the peak structure on the high-wavelength side, and extend to the distortions due to development of high-energy satellites via Coster-Kronig transitions and other processes. The exact structure will be dependent on factors such as detector resolution and other instrumental factors, for example, satellite intensity relative to diagram lines will be

dependent on beam energy (Rémond et al. 2002). Intensification of absorption edges must also be evaluated by direct measurement. The high-wavelength peak structure of a line such as $ThM\gamma$ will be exceptionally complex due to the influences of both low-energy core transitions, non-diagram line development, and the $M5$ absorption edge (see following section, below). It is critical to note that predicted line properties based on tabulations of X-ray data may not be appropriate in terms of either relative heights or positions and must be assessed specifically in the material being analyzed, within the context of the measurement parameters of the instrument being used.

The estimation of F (Eq. 3, above) based on symmetrical peaks and Gaussian profiles will not be appropriate for more difficult deconvolutions of interference scenarios such as $ThM\gamma$ (and family) on $UM\beta$, or of $YL\gamma_{2,3}$ on $PbM\alpha$, although it may have greater suitability when peak heights are similar. The application of $\lambda_r - \lambda_i$ to infer the magnitude of interference will also be affected by wavelength shifts caused by changes in atomic environment related to composition, especially where outer shell electrons are involved in at least one of the transitions producing the interfering diagram lines (as is the case of $YL\gamma_{2,3}$ and $PbM\alpha$). Furthermore, this approach relies on the correct determination of relative line heights between the measured and interfering peaks

Pb region - RT87-17

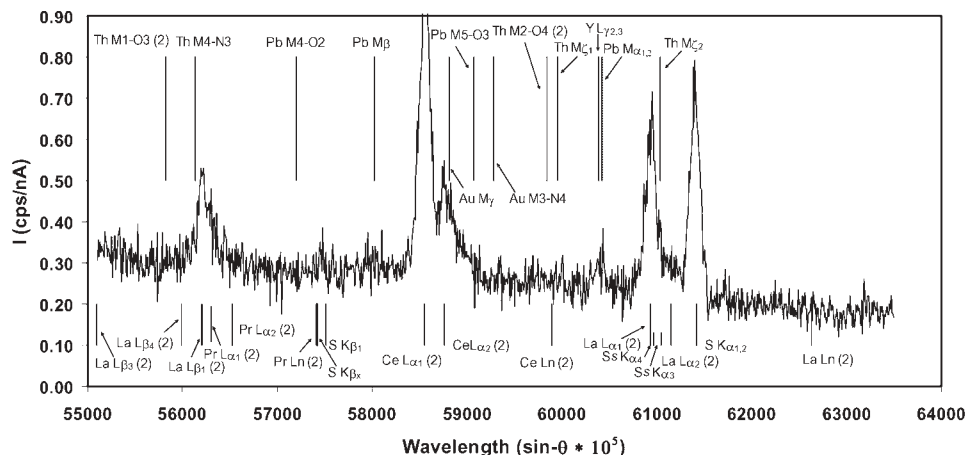


FIGURE 15. Wavelength scan of PbM region (PET) from monazite RT87-17. Note prominent sulfur peak. The S content in this monazite is approximately 0.3 wt%.

of the interfering element. Such a determination will only be reasonable where the peak heights can be directly related in the unknown, and where the interference is not mutual. Extending line-intensity ratios from other compositions (i.e., interference standards) requires scaling through matrix corrections, and becomes complex in cases of mutual absorption and fluorescence (Donovan et al. 1993).

The complication of peak position shift can influence both the above approach as well as those methods based on empirical corrections using measurements on standards containing high concentrations of the interfering element and none of the element of interest, such as suggested by Amlı and Griffen (1975), Gilfrich et al. (1978), and Pyle et al. (2002). We must emphasize that any interference corrections that are to be implemented must be based on measurements from the machine being used. No two spectrometers are exactly the same.

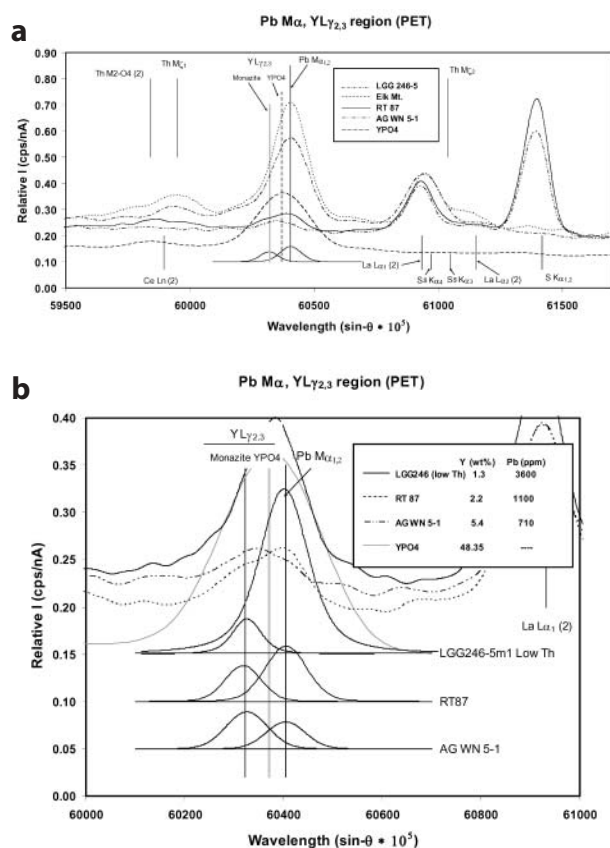


FIGURE 16. (a) Wavelength scans (after Savitsky-Golay noise filtering) of the $PbM\alpha$ region (PET) from several Y-bearing monazites and YPO_4 . Note S interference on the high-wavelength side of the second-order $LaLa\alpha$ peak. Initial deconvolution of RT87 spectrum indicates possible wavelength shift of $YL\gamma_{2,3}$ relative to the position in YPO_4 . The peak $YL\gamma_{2,3}$ position in YPO_4 corresponds well with cataloged positions in terms of the wavelength distance relative to $PbM\alpha$. (b) Detailed wavelength scans of Y-bearing monazites (0.00001 $\sin\theta$ steps, 6 s/step). Smoothed spectra have been positioned vertically for plotting but maintain true relative scale. Peak profiles (again, positioned arbitrarily for plotting) represent the results of background-subtracted deconvolution applying Voigt profiles. RT87, AG WN5-1, and LGG246 all give the same deconvoluted position $YL\gamma_{2,3}$ for relative to $PbM\alpha$.

Interferences relevant to $PbM\alpha$ measurement

The interference of Y on the $PbM\alpha$ line has been noted since the outset of attempts to analyze monazite for Pb with the electron microprobe. First-order $YL\gamma_{2,3}$ strongly overlaps the $PbM\alpha$ position, and must be accounted for in obtaining the correct Pb concentration, even though the Y concentration rarely exceeds 2 wt% in most monazites. Correcting interference based on line intensities obtained from either YPO_4 (Pb-free) or Y-Al garnet depend critically on the accuracy of matrix corrections as these materials differ substantially in overall composition. In addition, the precise peak position for $YL\gamma_{2,3}$ is expected to shift slightly as heavy elements substitute for Y in the lattice ($YL\gamma_{2,3}$ involves transitions from N2 and N3, the outermost filled shell). Even a slight positional shift can dramatically affect the severity of the overlap, depending on the resolution of the spectrometer in question.

The calculated interference of $YL\gamma$ based on reconciliation of $PbM\alpha$ vs $PbM\alpha$ on Elk Mt. monazite [$PbM\alpha$ is corrected for minor interference of $CeLa\alpha_1$ (2nd order)] gives a correction factor of 0.00195. This translates to a subtraction of 43 ppm on low Pb monazite RT87 (which contains 2.2 wt% Y and about 1100 ppm Pb). Deconvolution results closely agree, suggesting an overestimation of Pb (at the $PbM\alpha$ position) of 47 ppm. Note also that this deconvolution documents a shift in the $YL\gamma_{2,3}$ line to higher energy in monazite compared to the position in YPO_4 . As a further check on this deconvolution, two other monazite grains were scanned in detail, LGG246-5 (low-Th sector) and AGWN5-1 (Fig. 16). The deconvoluted peak positions match those of RT87-17, indicating a wavelength shift for $YL\gamma_{2,3}$ of about -4.5×10^{-3} Å in monazite relative to YPO_4 . This shift is qualitatively consistent with the suggestion that increasing bond length correlates with decreasing emission band wavelength (e.g., White and Gibbs 1969). REE-phosphate bond lengths are shorter in the tetragonal xenotime structure compared to the monoclinic monazite structure (Ni et al. 1995; Boatner 2002). If the correction for $YL\gamma_{2,3}$ is done by measurement of $PbM\alpha$ on Pb-free YPO_4 , followed by subtraction of raw intensity (based on the measured Y concentration) in the unknown without accounting for the wavelength shift, the Pb concentration would be overcorrected by a significant factor. We have quantified this shift based on the analysis of several monazite grains covering a range in Y concentration, with and without peak wavelength shift, and the overestimation is approximately 36 ppm Pb per wt% Y, in the range of 0.5 to 2.4 wt% Y (with 160 mm Rowland circle radius and PET). Using RT87-17, the resulting correction factor, based on the deconvoluted peak intensity contributions at the $PbM\alpha$ position (using the Y concentration from $YL\gamma$ measurement), gives a value of 0.002453. This factor will not scale directly to high Y concentration, however, due to both peak shape factors and possible wavelength shift.

Several studies have noted that $ThM\zeta_1$ and $M\zeta_2$ may interfere appreciably with $PbM\alpha$ (e.g., Sherrer et al. 2000; Pyle et al. 2002). Measured spectra on PET with a 160 mm Rowland circle radius do not clearly show this interference on $PbM\alpha$ except at high Th concentration (Fig. 17). This is not to say that the interference does not exist at lower Th concentration and certainly cannot be discounted completely. As this interference arises from the

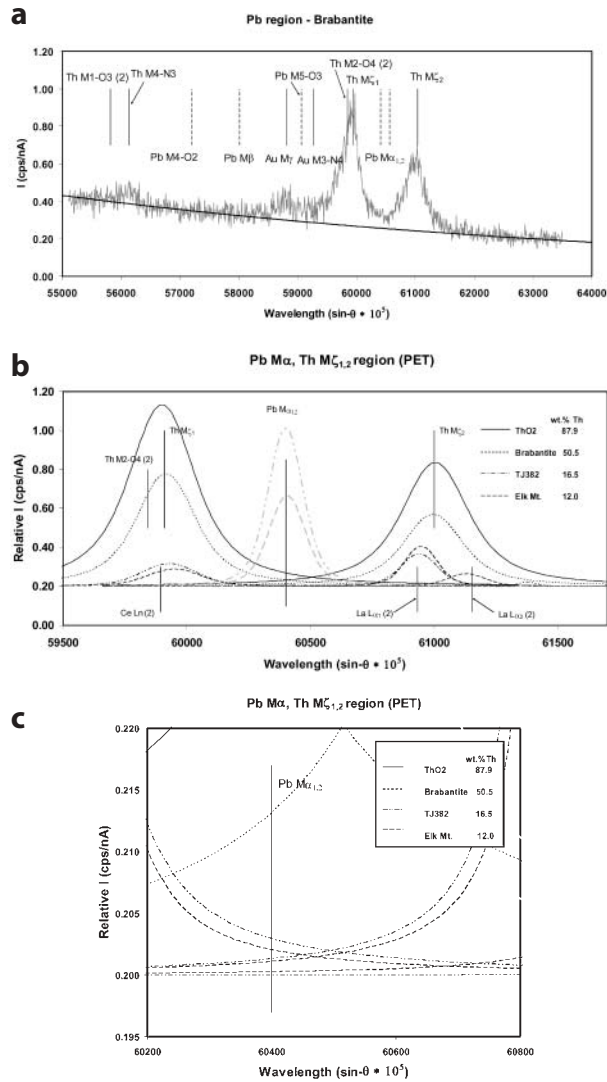


FIGURE 17. (a) Wavelength scan of PbM region (PET) from brabantite $[CaTh(PO_4)_2]$. Brabantite contains 50.5 wt% Th and the interference of the $ThM\zeta$ lines on $PbM\alpha$ is evident. (b) Deconvolution results of filtered (Savitsky-Golay) spectra showing detail of the $PbM\alpha$ region in monazites of different Th content. Deconvolution of $ThM\zeta_2$ from $LaLa_1$ (2nd order) is difficult without increasing the resolution during acquisition. These spectra were acquired with 0.00008 $\sin\theta$ steps, 1.5 s/step. (c) Detail of center portion of (b), showing overlaps of $ThM\zeta_1$ and $ThM\zeta_2+LaLa_1(2)$ on $PbM\alpha$.

distal peak tail structure of the Th lines on either side of $PbM\alpha$, the estimation of interference intensity will be highly dependent on the presumed peak profiles. Thorium interference on $PbM\alpha$ (primarily from $ThM\zeta_1$) contributes 785 ppm of apparent Pb in synthetic, Pb- and REE-free brabantite (50.22 wt% Th), and, from deconvolution of spectra, would suggest 49 ppm Pb at 16.5 wt% Th, and 34 ppm Pb at 12 wt% Th are contributed by $ThM\zeta_1$ (Fig. 17c). The contribution of $ThM\zeta_2$, though not easily deconvoluted from $LaLa_1(2)$, contributes 42% of the intensity of $ThM\zeta_1$ in brabantite, for a total contribution of 48 ppm to the Pb concentration at 12 wt% Th, and 70 ppm at 16.5 wt% Th. The

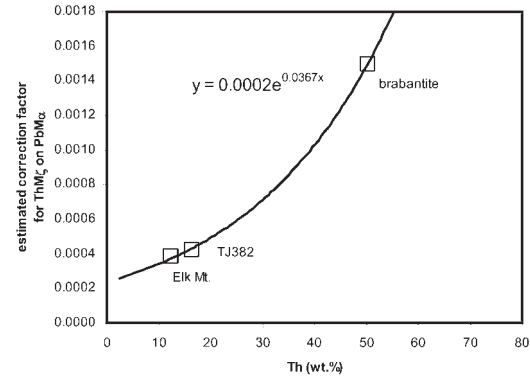


FIGURE 18. Estimated correction factor (see Eq. 1), and calculated best-fit, as a function of Th content, calculated from deconvolution. Note that these results are from scans obtained on 160 mm radius Rowland circle spectrometer and are specific to high-pressure (3 bars) P-10 counters.

resulting correction factor, which is therefore dependent on the Th concentration, is presented in Fig. 18. The magnitude of the interference for most monazite (2–6 wt% Th) will result in 5–18 ppm apparent Pb from Th interference on $PbM\alpha$.

Interferences relevant to $UM\beta$ measurement—actinide analysis

Uranium analysis in monazite, or in any Th-bearing material, is surely one of the more challenging measurements in micro-analysis outside the ultra-light element domain. This difficulty is due to strong overlaps on analytical lines, background complications from numerous interferences, and the appearance of absorption edges. The use of $UM\alpha$ as an analytical line has been generally abandoned because the overlap by $ThM\beta$ (and satellites) is exceptionally problematic, and is further complicated when Ar counters are used due to the appearance of the Ar-K absorption edge just below (in wavelength) $UM\alpha$ and $ThM\beta$, making background estimation particularly difficult. Although the resolution of $UM\beta$ from $ThM\gamma$ is assumed to be much better, this spectral region is also fraught with obstacles.

The accurate measurement of $UM\beta$ for geochronologic applications requires recognition and evaluation of the remarkable complexity of the wavelength region around $UM\beta$ resulting from the presence of significant Th. The calculated age, however, will be somewhat less sensitive to the U concentration as the relative amount of Th increases. Even in the case of very high Th contents (e.g., thorite or huttonite), it is unwise to consider inaccuracies in the U concentration to be of little overall consequence. As geochronology by EPMA continues to be refined and pushed to greater age sensitivity, great care must be exercised in this measurement. Thorium variation could be easily manifest as apparent age variation in cases where the Th-U overlap corrections are inadequate. As Th contents in monazite are typically several weight percent to well over 10 wt%, and, as revealed by mapping (Fig. 19), can cover an extraordinary compositional range even in small monazite grains, this is a non-trivial point.

Wavelength scans of the UM region in synthetic ThO_2 and $CaTh(PO_4)_2$ (brabantite) illustrate some of the Th-U complications (Fig. 20). The $ThM4$ and $M5$ absorption edges have a significant,

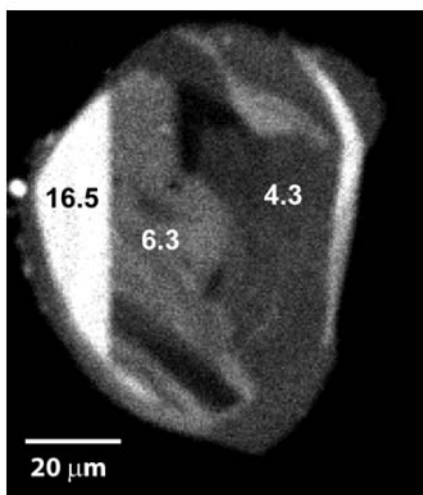


FIGURE 19. Thorium concentration map of monazite TJ382. Numbers are Th concentrations in wt%. Note domain structures are sharply defined, and that the concentration can vary by as much as a factor of 4 even in small monazite grains. Quantitative analysis requires accurate estimation of backgrounds (Th dependent) from each domain, and avoidance of domain boundaries to ensure homogeneous excitation volume.

visible effect on the spectrum at high-Th concentration (ThM α radiation originates from ionizations of the M5 level, and ThM β radiation originates from M4 ionizations, the edge height difference therefore behaves in accordance with the relative ionization probabilities, with the M5 edge slightly greater than the M4 edge). The ThM γ , M5-P3, and M3-N4 diagram lines will all interfere at

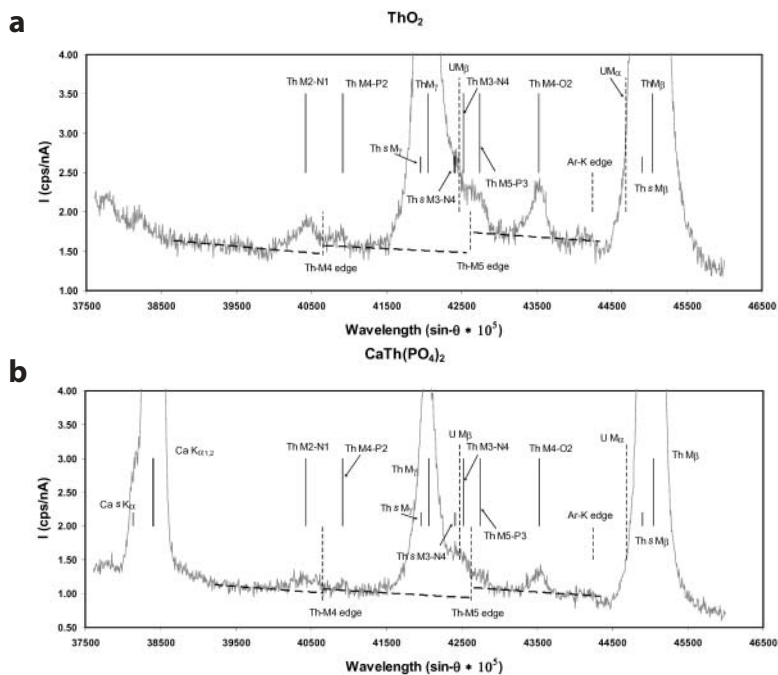


FIGURE 20. (a) Wavelength scan of the UM β region (PET) of synthetic ThO₂. Note complex interferences from Th on UM β as well as complications to potential background, importantly including the emergence of the ThM4 and M5 absorption edges. “s” indicates satellite lines. (b) Spectrum from synthetic (U-free) brabantite. Note typical broadening of peak structure on the low wavelength side of CaK α from satellite influence.

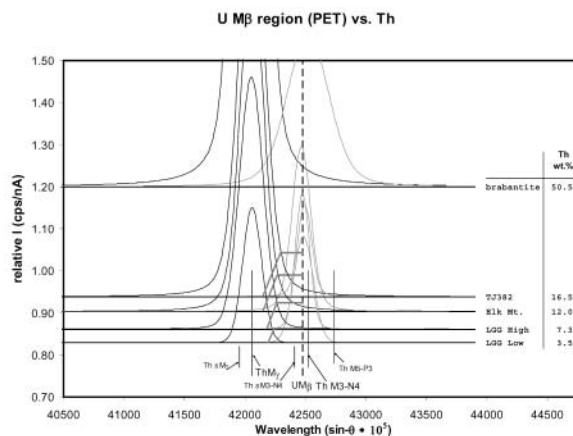


FIGURE 21. Deconvolutions of ThM γ from brabantite and monazite spectra. Profiles are placed positionally on the graph by relative Th content. The gray profile is the deconvoluted UM β +ThM3-N4 line. Separating Th M3-N4 from UM β is difficult, even with very detailed scanning. Heavy, gray horizontal lines mark the expected Th M3-N4 heights in the monazites predicted from the ThM γ /Th M3-N4 ratio in brabantite.

the UM β position. In addition, the ThM4-O2, M4-P2, and M2-N1 lines are major features that, along with the Th absorption edges, will influence background selection and estimation. The direct overlap of ThM3-N4 and UM β invalidates the application of interference corrections based on a symmetric ThM γ profile. Satellite structures superimposed on the low wavelength limbs of the main Th diagram lines complicate the overall UM β interference

contributions greatly. Therefore, the total structure of the spectrum imposed by Th must be considered when evaluating interference at the UM β position. The best method for evaluating the overall Th interference would be the measurement of apparent U (measured on UM β) in U-free, synthetic LREE monazite at varying Th content. Lacking this (to date), we can estimate a correction based on the peak structures of U-free ThO₂ and brabantite, scaled by the Voigt line shape of the ThM γ line, assuming that the ThM3-N4 diagram line and satellites will scale more or less linearly as a function of concentration (perhaps reasonable because this is essentially a direct overlap). UM β is not clearly deconvoluted from the mutual overlaps of ThM3-N4 and M5-P3. Assuming that the ThM3-N4 + M5-P3 contribution will scale proportionally with the ThM γ line, we can deconvolute monazite spectra (the UM β region) to evaluate the contribution of the ThM γ line (Fig. 21). Spectral deconvolution indicates that ThM γ in monazite with 3.5 wt% Th does not interfere with UM β (with a 160 mm Rowland circle), therefore the total interference at this Th concentration (or less) will arise from ThM3-N4 and M5-P3, and a relatively constant correction factor can be assumed until the ThM α line begins to interfere with UM β . At this point,

TABLE 4. Examples of recalculated U values using different correction factors (CF) for Th- UMβ overlap with differing Th, Pb, and U concentrations

| Th | Pb corr | U (uncorr) | CF = 0.008 | | CF = 0.0085 | | CF = 0.014 | |
|--------|---------|------------|------------|----------|-------------|----------|------------|----------|
| | | | U (corr) | age (Ma) | U (corr) | age (Ma) | U (corr) | age (Ma) |
| 125000 | 9098 | 5231 | 4232 | 1416 | 4169 | 1418 | 3481 | 1441 |
| 30000 | 987 | 5231 | 4991 | 475 | 4976 | 478 | 4811 | 481 |
| 5000 | 487 | 5231 | 5191 | 494 | 5189 | 494 | 5161 | 496 |
| 30000 | 987 | 600 | 360 | 701 | 345 | 702 | 180 | 714 |
| 30000 | 587 | 1200 | 960 | 396 | 945 | 396 | 780 | 403 |

All concentrations are given in ppm

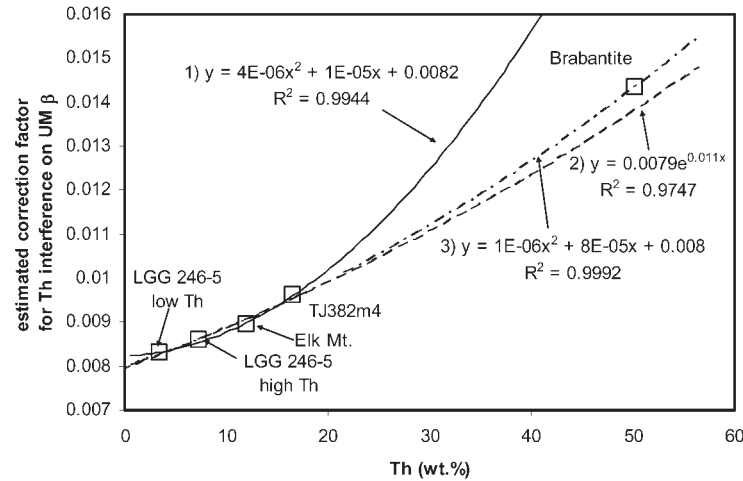


FIGURE 22. Calculated correction factors for the total Th interference on UMβ as a function of Th content. Curve 1 represents the polynomial fit of monazite points only. Curve 2 is the exponential fit of monazite points, curve 3 includes brabantite (polynomial). Figure 21 predicts that the correction factor should become constant at low Th wt% (below about 5 wt%) due to the lack of apparent interference of ThMγ on UMβ, such that the total interference at low-Th content is due to Th M3-N4. The exponential fit of monazite points is a better predictor for brabantite but the polynomial fit may be favorable if a constant correction factor at low-Th contents is argued. Note that the estimated correction factors tend to be higher than that predicted by simulated spectra (0.006) as reported by Pyle et al. (2002).

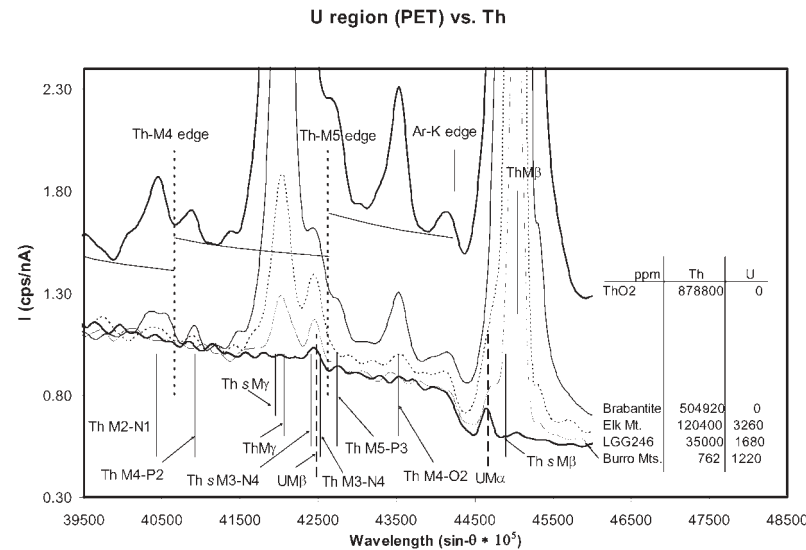


FIGURE 23. Smoothed wavelength spectra (UMβ region, PET) of synthetic ThO₂ and brabantite compared to natural monazites of varying Th content. Note the emergence of the ThM4 and M5 absorption edges that become very significant at high Th. The curves below the ThO₂ spectrum represent estimated background.

the correction must include the contribution of ThMα in addition to ThM3-N4 + M5-P3, and the total factor will increase (Figs. 21 and 22). The correction factor shifts from 0.0085 to near 0.008 between 12 wt% Th and 2 wt% Th. Although this produces significant shift in calculated U concentration, the calculated age tends to be less affected, as the age is primarily a function of Th/Pb (Table 4). However, if the U analysis is to be meaningful (and the age as accurate as possible), then the accuracy of the overlap correction must be carefully addressed on the particular instrument being used. Typically, U concentrations are around 0.1·Th or less in monazite, meaning that the U analysis is highly sensitive to Th overlap correction, which results in the subtraction of several hundred ppm U.

Strictly speaking, the true background appropriate to the measurement of UMβ lies between ThM4-P2 and ThMγ, with the background extending under the ThMγ family of lines up to the M5 edge. From a practical standpoint, the ThM4 and M5 edges will become inconsequential at low Th content, being largely dependent on the precision of the background measurement. The influence of the M5 edge is evident in wavelength scans of Th-bearing materials from about 12 wt% Th and above (Elk Mt. monazite, brabantite, ThO₂, Fig. 23), and appears non-resolvable at about 4 wt% Th. We can gauge the edge significance by estimating the expected Th concentration where we expect the edge in question to emerge from the background noise. Clearly, the more precisely the background is evaluated, the better the definition of the edge amplitude. A simple-minded approach would be to take “emergence from background noise” as defined by exceeding the Liebhafsky limit (Goldstein et al. 2003) of the background, that is, the point where the edge height exceeds the 3-σ level of the background (3N_{bkg})^{1/2}, where N_{bkg} represents the total background counts). Based on the edge heights estimated from brabantite, the M5 edge should be definable at about 3–4 wt% Th if the background precision (1σ) is near 0.5%, with the M4 edge emerging at nearly twice that concentration (Fig. 24).

As wavelength scans demonstrate (Fig. 23), the potential interferences around UMβ arising from Th alone are imposing, affecting

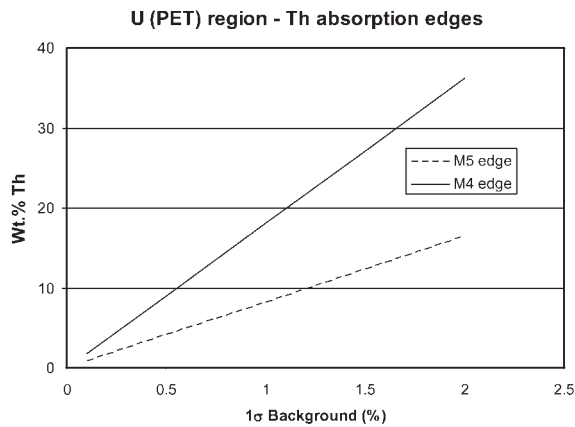


FIGURE 24. Estimated levels where the ThM4 and M5 absorption edge heights are expected to reach the “Liebhafsky limit,” i.e., 3σ level of the background ($3N_{\text{bkg}}^{1/2}$), as a function of background measurement precision and Th concentration.

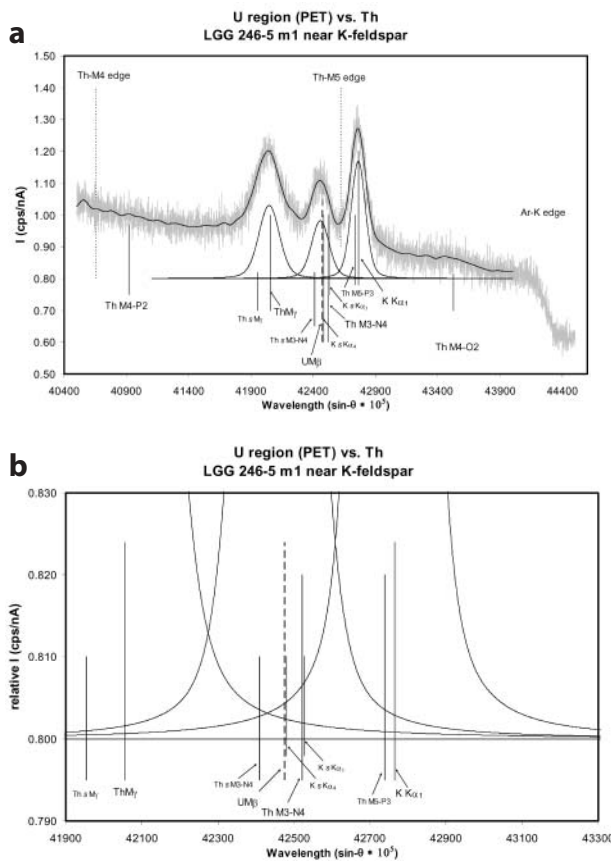


FIGURE 25. (a) Potassium interference on $UM\beta$. This wavelength spectrum (PET) is from monazite from the Lower Granite Gorge of the Grand Canyon and was taken at the rim of the monazite a few micrometers from the interface with K-feldspar. Mutual interferences make this correction particularly problematic. Note that at high-Th concentration (the Th concentration is about 4 wt% here), the interference of $KK\alpha$ and ThM5-P3 will not permit a simple K measurement and correction. (b) Detail of interference at the $UM\beta$ position.

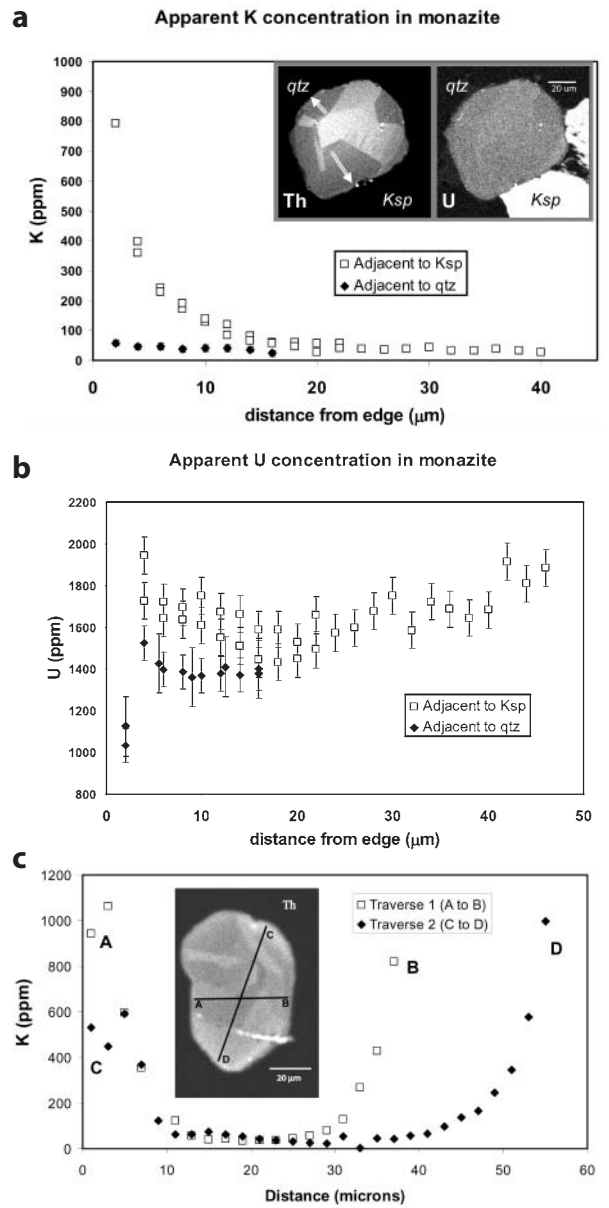


FIGURE 26. Potassium fluorescence effects in LGG246-5m1 and m2 monazite grains. (a) Apparent K concentrations in Grain m1 near monazite rim adjacent to K-feldspar compared to the rim next to quartz. (b) Uranium concentrations (Th overlap corrected) from m1. (c) Apparent K concentrations along point traverses in grain m2 which is completely included in K-feldspar, the apparent K (and therefore spurious U at the $UM\beta$ position) are seen to increase toward the rim in all directions. The apparent K is produced by fluorescence by REE L radiation (from the K-feldspar).

both the measured $UM\beta$ peak intensity as well as complicating background selection. Selecting spectral regions to include in background estimation becomes increasingly difficult with increasing Th content due to both the emergence of absorption edges (discussed above), as well as the increase in intensity of the ThM4-O2, M4-P2, and M2-N1 diagram lines. Although barely visible in spectra from monazite containing less than 4 wt%

Th (Fig. 23), high-precision counting necessitates the complete avoidance of these lines during background acquisition, for example, the emergence of ThM4-O2 renders the region between 0.43300 and 0.43800 $\sin\theta$ unusable at Th contents greater than about 10 wt%.

Fluorescence interferences

Despite even the most careful consideration of interferences, the occurrence of even minor amounts of unexpected elements, such as S (see Fig. 15), can have substantial consequences for trace-element analysis. In addition, and at least as significant, are interferences arising from fluorescence of X-rays from high-concentration elements in minerals adjacent to the phase being analyzed. The discussion of U measurement in the presence of Th (above) becomes even more complex when K becomes detectable, as the first order $KK\alpha$ diagram line occurs on the high wavelength side of $UM\beta$ (Fig. 25). Because $KK\alpha$ is easily fluoresced by LREE L -radiation, monazite hosted by K-feldspar or K-mica requires prudent consideration of the effect of this line, especially as analyses near grain edges (to assess overgrowths) are attempted. Potassium $K\alpha$ will begin to interfere with $UM\beta$ at apparent concentrations as low as 100 ppm, but, like the low intensity Th lines mentioned above, it is important to keep in mind that at any detectable level there is potential interference at high-wavelength $UM\beta$ background positions. Whether fluoresced or actually present in some monazite, K presents a good example of the kinds of unexpected spectral complexity that can substantially compromise age results. Scanning the spectrum around the peaks of interest allows a direct visual evaluation by which the presence and severity of some interferences on characteristic lines and/or background regions can be judged. In cases where background interference exists, more appropriate regions can then be selected for intensity estimation.

Monazite LGG246-5 m1 from the Lower Gorge of the Grand Canyon illustrates how fluorescence of K can affect geochronologic EPMA. As shown in a detailed $UM\beta$ -region wavelength scan from the lower-right rim of this monazite where it contacts

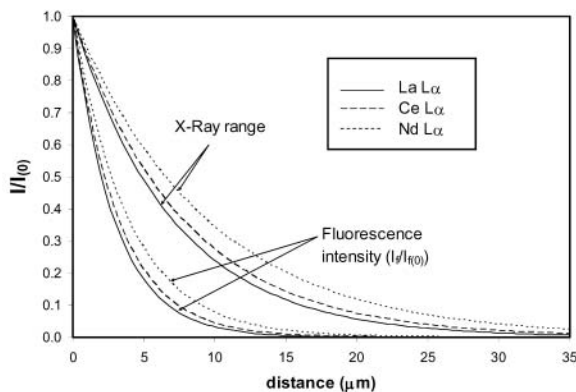


FIGURE 27. Estimated X-ray range for LREE in monazite approximated using photon attenuation theory with a weight fraction-based (LGG246-5 m1, low-Th domain composition), bulk mass-absorption coefficient (Goldstein et al. 2003), and fluorescence intensity vs. distance [$I_f/I(0)$] from a vertical interface in monazite, estimated using the approximation method of Reed (1993). The assumed density for monazite is 5 g/cm³.

K-feldspar (Fig. 25), the $KK\alpha$ line forms a prominent feature several micrometers within the monazite. As Th, U, and K mutually overlap, this is particularly difficult scenario.

Trace-element analyses across this monazite illustrate the magnitude of the K fluorescence effect on both the apparent U concentration and the resulting age estimation (Figs. 26 and 28). Note that the analyses near the K-feldspar are from within a generally low-Th sector and that there is a similar low-Th sector in the upper-left corner of this grain adjacent to quartz, allowing good analytical control. Analyses of K within monazite (without correcting for the potential interferences of $UM\beta$ and ThM5-P3) are shown in Figure 26a. Potassium becomes detectable approximately 10–15 μm from the interface with K-feldspar, and increases exponentially toward the rim. Analyses approaching the rim next to quartz show no such trend. Analyses of U (using $UM\beta$, with only Th overlap corrections), also increase toward the rim next to K-feldspar, inverting the general trend toward lower U toward the rim (Fig. 26b). The reversal in trend corresponds to the increasing apparent K concentration. Note that the trend in the domain adjacent to quartz is flat or has a possible decrease in U concentration toward the rim. Figure 26c shows the apparent K concentrations in a monazite grain (m2) from the same sample, illustrating that there is no dependence on spectrometer/grain boundary relationship. X-rays arising from L ionizations in REE maintain significant intensity from the primary excitation volume to more than 20 μm in monazite, and the apparent magnitude of the K fluorescence effect is consistent with the estimation of fluorescence intensity as a function of distance from a vertical boundary (Fig. 27). The resulting age estimates are striking (Fig. 28). The apparent increase in U toward the rim adjacent to K-feldspar leads to a reduction in the apparent age, by as much as 100 m.y. relative to the predominant age estimates elsewhere in this grain. Again, the domain adjacent to quartz exhibits a flat age profile, in excellent agreement with the ages calculated for the rest of this sector-zoned monazite. Clearly, the effect of K fluorescence at the rim is a major factor that could, if unaccounted for, lead to misinterpretation of the apparent concentrations and the conclusion that the monazite is substantially younger on the rim. Any monazite rim analyses

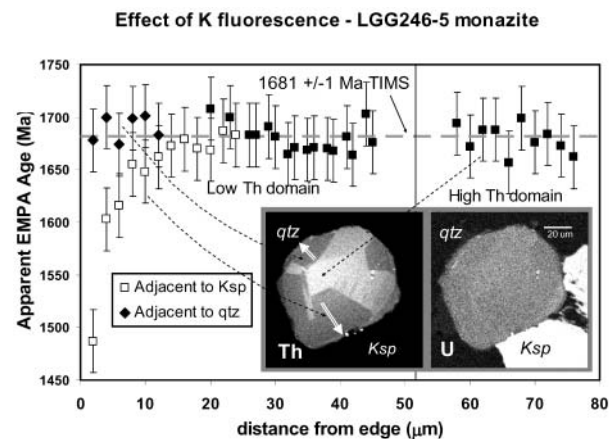


FIGURE 28. Calculated ages for points in Figure 26. Potassium interference causes a strong underestimation of age near the rim. Note 1681 ± 1 via IDTIMS from monazite from this sample (K. Davidek and S. Bowring, personal communication).

in K-feldspar or K-mica hosted monazite must carefully contend with this issue. At a minimum, trace analysis for K is indicated when using the $UM\beta$ line for U analysis.

SUMMARY AND DISCUSSION

Tectonic histories typically involve multiple episodes of mineral growth and deformation, and microanalysis offers hope for deciphering these complexities as polygenetic monazite or xenotime may exist in a single sample, or even in a single grain (Montel et al. 1996; Cocherie et al. 1998; Crowley and Ghent 1999; Williams et al. 1999; Terry et al. 2000; Williams and Jercinovic 2002). However, apparently minor analytical effects can have major manifestations in resulting concentration measurements and age estimates, and inaccuracies in analysis can potentially lead to tempting interpretations or require proposing tortuous (and unfounded), ad-hoc geochemical or tectonic chimera. Not only will analytical errors produce erroneous age results, but eventually an erroneous impression of the accuracy of the technique will also emerge. Thorough investigation of all aspects of data acquisition and a better understanding of the origin and behavior of the relevant accessory minerals is required. To this point, experimental work indicates that bulk Pb diffusion, even at elevated temperatures, is a very slow process in monazite, allowing a complex record of polymetamorphism potentially to be preserved (Cherniak et al. 2004; Seydoux-Guillaume et al. 2002a). The thermodynamic relationships controlling accessory phase growth during prograde metamorphism, element parti-

tioning, the role of fluids in monazite decomposition and reprecipitation reactions, along with the associated thermobarometric implications are also being established (Andrehs and Heinrich 1998; Heinrich et al. 1997; Gratz and Heinrich 1997, 1998; Teufel and Heinrich 1997; Pyle and Spear 1999; Seydoux-Guillaume et al. 2002b; Spear and Pyle 2002; Wing et al. 2003).

The application of the electron microprobe to trace-element analysis offers enormous potential both in geochemistry and geochronology, however, there are many analytical challenges that go significantly beyond what is generally necessary for major-element analysis. Certainly, rigorous evaluation of such aspects as the relevant physical constants and matrix algorithms will ultimately be necessary. Very high quality thin section preparation is a necessary starting point because features such as poor polish or high physical relief will result in difficult or impossible grain edge analysis as well as conductivity problems. Instrumental variables such as counter gas pressure variation, dead time corrections, and current measurement linearity (does the calibration at low current and analysis at high current correspond in the current normalization?) all introduce another level of complexity, but must be clearly evaluated and controlled. Careful pulse-height analysis is critical for minimizing high-order interference effects but, as noted by Lifshin and Gauvin (2001), care must be taken not to constrain the energy windows such that counts are lost at high count rates (see Pyle et al. 2005, this volume). For this reason, we recommend setting PHA parameters based on counter energy distributions for the peaks of interest on standards with

TABLE 5. Summary of analytical procedure for EMPA geochronology as currently implemented at UMass

| Step | Procedure | Explanation |
|------|--|--|
| 1 | Full section map | Carbon coat thin section (vacuum evaporation to ~250 Å) and collect map of Ce (and/or La), along with base-map reference element (Mg, Al). Typically 1024 × 512 pixels, 35 μm pixel step size, defocused beam (~35 μm). 350 nA, 15 kV, 10 ms count time/pixel. |
| 2 | Process maps for accessory mineral selection | Import raw maps into image analysis program (Adobe Photoshop or equivalent). Adjust I/O levels to highlight Ce (or La) spots and import adjusted maps as layers into Adobe Illustrator or equivalent. Mark spots from REE maps on separate layer with circles, dots, etc. Overlay marked layer on base map (Mg or Al) to identify accessory phases in textural context. |
| 3 | Map minerals at high magnification | Map selected grains, usually beam rastering at resolution giving step size <1 μm. Generally YLa, ThMa, $UM\beta$, and PbMa, (and/or other geochemically important elements). 200 nA, 100 ms, focused beam. |
| 4 | Generate age maps | Estimate pixel U, Th, Pb, and U concentrations in high-magnification maps by producing <i>k</i> -ratios (subtract background intensities, reference to standard intensities), then applying matrix correction factors. Calculate age values by iteration of age equation, then re-assemble pixels into "age map". |
| 5 | Collect major element analyses | Run major element analyses, 15 nA, 15 kV, focused beam, of monazite, xenotime, etc. Should collect analyses from all domains identified in maps (step 3 above). |
| 6 | Remove carbon coat, then apply gold coat | Lightly polish section (≤0.3 μm polishing compound) to remove C-coat. Apply Au coat to thin section(s) and standards (stripped of coatings) by vacuum evaporation. Should be ≥80 Å. |
| 7 | Collect backgrounds for trace element analysis | Acquire wavelength scans of regions around YLa, ThMa, $UM\beta$, and PbMa (8-sinθ steps over 8400 sinθ range, 1500 ms/step, 200 nA, 15 kV, focused beam, differential mode PHA). Collected counts are converted to dead-time corrected cps/nA. Backgrounds should be acquired for each identified compositional domain, particularly guided by thorium variation. |
| 8 | Extract background intensity from scans | Apply digital noise filter to scan data, select appropriate background regions (avoiding interferences), and regress included data (exponential or polynomial best-fit). Apply regressed line to peak position to calculate intensity of background. |
| 9 | Obtain trace element analyses | Enter background intensities into analysis definitions along with appropriate major element concentrations. Calibrate (at 15 nA, 15 kV, focused beam), YLa, ThMa, $UM\beta$, and PbMa, then analyze unknowns (200 nA, 15 kV, focused beam, 600–900 s per point). Identified compositional domains should be individually analyzed. Multiple analyses within a domain increases the precision on the age estimate as evaluated via the standard error of the mean. Concentrations are modified by empirical corrections for overlaps. Such corrections are done by either 1) use of correction factors calculated by spectral measurement and deconvolution, or by measuring Pb in Pb-free YPO ₄ , (accounting for the wavelength shift of YLγ between YPO ₄ and monazite) and brabantite, and by measuring U in brabantite, scaling the intensity according to the matrix to be able to subtract counts at the <i>k</i> -ratio level, then running corrected intensities through the matrix procedure (PAP in this case). |
| 10 | Calculate ages | Calculate Pb as a function of age, Th, and U concentrations. By iteration of age, converge to the measured Pb concentration. |

relatively high concentrations, or, as in the case of high-Th monazite, to set parameters based on the highest count rate scenario to be encountered for that element either during calibration or analysis. As Lifshin and Gauvin (2001) also pointed out, errors generated by differences in quantitative models will be strongly dependent on absorption parameters, in turn a function of both the composition of the sample and the beam voltage. For this reason, as well as effects of spatial resolution, users must balance the benefits of high overvoltage to enhance precision, against the potential resulting inaccuracies. We select 15 kV in order to have sufficient overvoltage to count Th, U, and Pb, and, at the same time, minimize the interaction volume, in accordance with the work of Montel et al. (1996).

In most monazite, compositional variation is most significant for Th and Y at the major-element level, and the assumption of constant REE ratios (the measured range generally is within a few percents for most monazite in a sample) is reasonable for matrix corrections (see quantitative discussion by Pyle et al. 2005, this volume). Obviously, this assumption will break down at some level, meaning that the highest accuracy analyses should have major elements included in the complete analysis of each point. Although this is largely impractical at present, a survey of major-element compositions should be obtained by taking several analyses from each domain identified by mapping prior to quantitative analysis. At the very least, the analyst will then be alerted to major substitutional trends or the presence of otherwise unexpected elements (as in the case of As presented here).

Careful X-ray mapping and wavelength scanning are essential for accurate analysis. Maps reveal zoning patterns and indicate the extent of domains within and among grains to be analyzed, guiding background acquisition and quantitative analysis. The quantitative strategy must be guided by maps, or point placement on domain boundaries or within domains with compositions inappropriate to the backgrounds being employed, are inevitable, resulting in high scatter and potential inaccuracy. Wavelength scans reveal the background shape and detail features of interferences relevant to both peak and background measurement. Such scans offer an explicit means to estimate the true background to be subtracted from peak intensity measurements, and can, if sufficiently detailed, offer a means to evaluate overlaps. Table 5 lists the overall technique for EPMA geochronology presently used at UMass.

ACKNOWLEDGMENTS

The authors owe a special thanks to Jean-Claude Dousse, whose advice and guidance in navigating X-ray spectra in general, and aid in interpretation of the uranium spectral region in spectra from ThO₂ and brabantite in particular, was invaluable. Frank Spear, Joe Pyle, and Bob Tracy all provided thorough and very helpful reviews. We owe a great debt of gratitude to all those whom have provided materials or consented to have data used, including Michael Bersch, who provided the Elk Mt. monazite; Peter Dahl, who supplied many samples from the Black Hills and Tobacco Root mountains, some of which have provided the inspiration for looking deeper into X-ray spectra than any of us originally anticipated; Jeff Amato supplied low thorium monazite from the Burro Mts.; Robert Berman, supplied section TJ382 (from Canada); Art Goldstein supplied section AG-WN5-1; The Tusas Mts., NM high arsenic monazite was part of Peter Davis' MS thesis research; Robert Tucker generously provided mineral separates from Norway (and elsewhere); Jean-Marc Montel supplied synthetic, Pb-free REE phosphates; Virginia Gillerman supplied samples (monazite-thorite) from the Lemhi Pass Th district in Idaho. Julie Baldwin, Kathy Davidek, and Sam Borving at MIT provided IDTIMS analyses of the Elk Mt. monazite, as well as LGG246-5 (Lower Granite Gorge of the Grand Canyon). Philippe Goncalves offered numerous helpful suggestions for the manuscript. This work was supported by NSF Grant EAR-0004077.

REFERENCES CITED

- Åmli, R. and Griffen, W. (1975) Microprobe analysis of REE minerals using empirical correction factors. *American Mineralogist*, 60, 599–606.
- Andrehs, G. and Heinrich, W. (1998) Experimental determination of REE distributions between monazite and xenotime. *Chemical Geology*, 149, 83–96.
- Armstrong, B.H. (1967) Spectrum line profiles: The Voigt function. *Journal of Quantitative Spectroscopy Radiation Transfer*, 7, 61–88.
- Asami, M., Suzuki, K., and Grew, E.S. (2002) Chemical Th-U-total Pb dating by electron microprobe analysis of monazite, xenotime and zircon from the Archean Napier Complex, East Antarctica: Evidence for ultra-high-temperature metamorphism at 2400 Ma. *Precambrian Research*, 114, 249–275.
- Boatner, L.A. (2002) Synthesis, structure, and properties of monazite, pretilite, and xenotime. In M.J. Kohn, J. Rakovan, and J.M. Hughes, Eds., *Phosphates: Geochemical, Geobiological, and Materials Importance*, 148, 87–121. *Reviews in Mineralogy and Geochemistry Mineralogical Society of America*, Washington, D.C.
- Bolz, R.E. and Tuve, G.L. (1976) *CRC Handbook of Tables of Applied Engineering Science*. CRC Press, Cleveland. 1184 pp.
- Bowles, J.F.W. (1990) Age dating of individual grains of uraninite in rocks from electron microprobe analyses. *Chemical Geology*, 83, 47–53.
- Cheong, C.-S., Jeong, G.-Y., Kim, H., Choi, M.-S., Lee, S.-H., and Cho, M. (2002) Early Permian peak metamorphism recorded in U-Pb system of black slates from the Ogecheon metamorphic belt, South Korea, and its tectonic implication. *Chemical Geology*, 193, 81–92.
- Cherniak, D.J., Watson, E.B., Grove, M., and Harrison, T.M. (2004) Pb diffusion in monazite: A combined RBS/SIMS study. *Geochimica et Cosmochimica Acta*, 68, 829–840.
- Cocherie, A. and Albarede, F. (2001) An improved U-Th-Pb age calculation for electron microprobe dating of monazite. *Geochimica et Cosmochimica Acta*, 65, 4509–4522.
- Cocherie, A., Legendre, O., Peucat, J.J., and Kouamelan, A.N. (1998) Geochronology of polygenetic monazites constrained by in situ electron microprobe Th-U-total lead determination: Implications for lead behavior in monazite. *Geochimica et Cosmochimica Acta*, 62, 2475–2497.
- Crowley, J.L. and Ghent, E.D. (1999) An electron microprobe study of the U-Th-Pb systematics of metamorphosed monazite: The role of Pb diffusion versus overgrowth and recrystallization. *Chemical Geology*, 157, 285–302.
- Dahl, P.S., Hamilton, M.A., Terry, M.P., Jercinovic, M.J., Williams, M.L., and Frei, R. (2005) Comparative geochronometry of metamorphic monazite in the eastern Wyoming province (USA), with implications for electron microprobe dating of Proterozoic thermotectonism. *American Mineralogist*, 90, {ERIC FILL IN}
- Donovan, J.J. and Tingle, T.N. (1996) An improved mean atomic number correction for quantitative microanalysis. *Journal of Microscopy*, 21, 1–7.
- Donovan, J.J., Snyder, D.A., and Rivers, M.L. (1993) An improved interference correction for trace element analysis. *Microbeam Analysis*, 2, 23–28.
- Fialin, M., Rémy, H., Richard, C., and Wagner, C. (1999) Trace element analysis with the electron microprobe: New data and perspectives. *American Mineralogist*, 84, 70–77.
- Fiori, C.E., Myklebust, R.L., Heinrich, K.F.J., and Yakowitz, H. (1976) Prediction of continuum intensity in energy-dispersive X-ray microanalysis. *Analytical Chemistry*, 48, 172–176.
- Förster, H.J., Harlov, D., and Milke, R. (2000) Composition and Th-U-total Pb ages of huttonite and thorite from Gillespie's beach, South Island, New Zealand. *Canadian Mineralogist*, 38, 675–684.
- French, J.E., Heaman, L.M., and Chacko, T. (2002) Feasibility of chemical U-Th-total Pb baddeleyite dating by electron microprobe. *Chemical Geology*, 188, 85–104.
- Geisler, T. and Schleicher, H. (2000) Improved U-Th-total Pb dating of zircons by electron microprobe using a simple new background modeling procedure and Ca as a chemical criterion of fluid-induced U-Th-Pb discordance in zircon. *Chemical Geology*, 163, 269–285.
- Geller, J.D. and Herrington, C. (2002) High count rate electron probe microanalysis. *Journal of Research of the National Institute of Standards and Technology*, 107, 503–508.
- Gilfrich, J.V., Birks, L.S., and Criss, J.W. (1978) Correction for line interferences in wavelength-dispersive X-Ray analysis. In T.G. Dzubay, Ed., *X-Ray Fluorescence Analysis of Environmental Samples*, p. 283–288. *Ann Arbor Science Publishers*, Michigan.
- Goldstein, J., Newbury, D., Joy, D., Lyman, C., Echlin, P., Lifshin, E., Sawyer, L., and Michael, J. (2003) *Scanning Electron Microscopy and X-Ray Microanalysis*, 3rd ed., 689 p. Kluwer Academic/Plenum, New York.
- Gratz, R. and Heinrich, W. (1997) Monazite-xenotime thermobarometry II: Experimental calibration of the miscibility gap in the binary system CePO₄-YPO₄. *American Mineralogist*, 82, 772–780.
- (1998) Monazite xenotime thermometry III. Experimental calibration of the partitioning of gadolinium between monazite and xenotime. *European Journal of Mineralogy*, 10, 579–588.
- Gunn, J.S., Harrowfield, I.R., Proctor, C.H., and Thresher, R.E. (1992) Electron

- probe microanalysis of fish otoliths—evaluation of techniques for studying age and stock discrimination. *Journal of Experimental Marine Biology Ecology*, 158, 1–36.
- Heinrich, W., Andrehs, G., and Franz, G. (1997) Monazite—xenotime thermometry. I: An empirical calibration. *Journal of Metamorphic Geology*, 15, 3–16.
- Hölzer, G., Fritsch, M., Deitsch, M., Härtwig, J., and Förster, E. (1997) *Physical Reviews A*, 56, 4554–4568.
- Horowitz, P. and Hill, W. (1989) *The Art of Electronics*, 1125 pp. Cambridge University Press, Cambridge.
- Ida, T., Ando, M., and Toraya, H. (2000) Extended pseudo-Voigt function for approximating the Voigt profile. *Journal of Applied Crystallography*, 33, 1311–1316.
- Kempe, U. (2003) Precise electron microprobe age determination in altered uraninite: Consequences on the intrusion age and the metallogenic significance of the Kirchberg granite (Erzgebirge, Germany). *Contributions to Mineralogy and Petrology*, 145, 107–118.
- Kerrick, D.M., Eminhizer, L.B., and Villaume, J.F. (1973) The role of carbon film thickness in electron microprobe analysis. *American Mineralogist*, 58, 920–925.
- Kramers, H.A. (1923) On the Theory of X-ray Absorption and of the Continuous X-ray Spectrum. *Philosophical Magazine*, 46, 836–871.
- Lifshin, E., Ciccarelli, M.F., and Bolon, R.B. (1975) X-Ray spectral measurement and interpretation. In J.I. Goldstein and H. Yakowitz, Eds., *Practical Scanning Electron Microscopy, Electron and Ion Microprobe Analysis*, p. 263–297. Plenum Press, New York.
- Lifshin, E. and Gauvin, R. (2001) Minimizing errors in Electron Microprobe Analysis. *Microscopy and Microanalysis*, 7, 168–177.
- Lumpkin, G.R. and Chakoumakos, B.C. (1988) Chemistry and radiation effects of thorite-group minerals from the Harding pegmatite, Taos County, New Mexico. *American Mineralogist*, 73, 1405–1419.
- Montel, J.M., Foret, S., Veschambre, M., Nicollet, C., and Provost, A. (1996) Electron microprobe dating of monazite. *Chemical Geology*, 131, 37–53.
- Ni, Y., Hughes, J.M., and Mariano, A.N. (1995) Crystal chemistry of the monazite and xenotime structures. *American Mineralogist*, 80, 21–26.
- Parrish, R. (1990) U-Pb dating of monazite and its application to geological problems. *Geological Survey of Canada Contribution* 12090, 1431–1450.
- Parslow, G.R., Brandstätter, F., Kurat, G., and Thomas, D.J. (1985) Chemical ages and mobility of U and Th in analcites of the Cree Lake zone, Saskatchewan. *Canadian Mineralogist*, 23, 543–551.
- Press, W.H., Teukolsky, S.A., Vetterling, W.T., and Flannery, B.P. (2002) *Numerical Recipes in C++: The Art of Scientific Computing*, 1032 p. Cambridge University Press, Cambridge, U.K.
- Pyle, J.M. and Spear, F.S. (1999) Yttrium zoning in garnet: Coupling of major and accessory phases during metamorphic reactions. *Geological Materials Research*, 1, 1–49.
- Pyle, J.M., Spear, F.S., and Wark, D.A. (2002) Electron microprobe analysis of REE in Apatite, Monazite, and Xenotime: Protocols and Pitfalls. In M.J. Kohn, J. Rakovan, and J.M. Hughes, Eds., *Phosphates: Geochemical, Geobiological, and Materials Importance, Reviews in Mineralogy and Geochemistry*, 48, 337–362. Mineralogical Society of America, Washington.
- Pyle, J.M., Spear, F.S., Wark, D.A., Daniel, C.G., and Storm, L.C. (2005) Contribution to precision and accuracy of chemical ages of monazite. *American Mineralogist*, 90, 547–577.
- Reed, S.J.B. (1993) *Electron Microprobe Analysis* (2nd ed.), 326 p. Cambridge University Press, Cambridge.
- Rémond, G., Myklebust, R., Fialin, M., Nockolds, C., Phillips, M., and Roques-Carnes, C. (2002) Decomposition of Wavelength Dispersive X-Ray Spectra. *Journal of Research of the National Institute of Standards and Technology*, 107, 509–529.
- Rhede, D., Wendt, I., and Förster, H.-J. (1996) A three-dimensional method for calculating independent chemical U/Pb- and Th/Pb-ages of accessory minerals. *Chemical Geology*, 130, 247–253.
- Roeder, P.L. (1985) Electron-microprobe analysis of minerals for rare-earth elements: Use of calculated peak-overlap corrections. *Canadian Mineralogist*, 23, 263–271.
- Savitsky, A. and Golay, M.J.E. (1964) Smoothing and differentiation of data by simplified least squares procedures. *Analytical Chemistry*, 36, 1627–1639.
- Scherer, N.C., Engi, M., Gnos, E., Jakob, V., and Liechti, A. (2000) Monazite analysis; from sample preparation to microprobe age dating and REE quantification. *Schweizerische Mineralogische und Petrographische Mitteilungen*, 80, 93–105.
- Seydoux-Guillaume, A.M., Paquette, J.L., Wiedenbeck, M., Montel, J.M., and Heinrich, W. (2002a) Experimental resetting of the U-Th-Pb system in monazite. *Chemical Geology*, 191, 165–181.
- Seydoux-Guillaume, A.M., Wirth, R., Heinrich, W., and Montel, J.M. (2002b) Experimental determination of the Th partitioning between monazite and xenotime using analytical electron microscopy. *European Journal of Mineralogy*, 14, 869–878.
- Small, D.G.W., Leigh, S.D., Newbury, D.E., and Myklebust, R.L. (1987) Modeling of the bremsstrahlung radiation produced in pure-element targets by 10–40 keV electrons. *Journal of Applied Physics*, 61, 459–469.
- Spear, F.S. and Pyle, J.M. (2002) Apatite, monazite, and xenotime in metamorphic rocks. In M.J. Kohn, J. Rakovan, and J.M. Hughes, Eds., *Phosphates: Geochemical, Geobiological, and Materials Importance*, 48, 291–335. Reviews in Mineralogy and Geochemistry Mineralogical Society of America, Washington, D.C.
- Spray, J.G. and Rae, D.A. (1995) Quantitative electron-microprobe analysis of alkali silicate glasses: A review and user guide. *Canadian Mineralogist*, 33, 323–332.
- Stormer, J.C., Jr., Pierson, M.L., and Tacker, R.C. (1993) Variation in F and Cl X-ray intensity due to anisotropic diffusion in apatite during electron microprobe analysis. *American Mineralogist*, 78, 641–648.
- Suzuki, K. and Adachi, M. (1991) Precambrian provenance and Silurian metamorphism of the Tsubonosawa paragneiss in the South Kitakami terrane, Northeast Japan, revealed by the chemical Th-U-total Pb isochron ages of monazite, zircon, and xenotime. *Geochemical Journal*, 25, 357–376.
- — — (1998) Denudation history of the high T/P Ryoke metamorphic belt, southwest Japan: Constraints from CHIME monazite ages of gneisses and granulites. *Journal of Metamorphic Geology* 16, 23–37.
- Terry, M.P., Robinson, P., Hamilton, M.A., and Jercinovic, M.J. (2000) Monazite geochronology of UHP and HP metamorphism, deformation, and exhumation, Nordoyane, Western Gneiss Region, Norway. *American Mineralogist*, 85, 1651–1664.
- Teufel, S. and Heinrich, W. (1997) Partial resetting of the U-Pb isotope system in monazite through hydrothermal recrystallization: An SEM and U-Pb isotope study. *Chemical Geology*, 137, 273–281.
- Tucker, R.D., Krogh, T.E., and Råheim, A. (1990) Proterozoic evolution and age-province boundaries in the central part of the Western Gneiss Region, Norway: Results of U-Pb dating of accessory minerals from Trondheimsfjord to Geiranger. In C.F. Gower, T. Rivers, and B. Ryan, Eds., *Mid-Proterozoic Laurentia-Baltica*, 38, 149–173. Geological Association of Canada, Special Paper. St. John's, Canada.
- Walker, J.M. and Howitt, D.G. (1986) Alkali metal loss in glass from a characterizing electron probe. In A.D. Romig and W.F. Chambers, Eds., *Microbeam Analysis—1986*, p. 299–301. San Francisco Press, Inc.
- Wallace, P. and Carmichael, I.S.E. (1992) Oxidation state of sulfur in submarine glassy lavas as determined by electron microprobe. *EOS* 73, 607.
- Ware, N.G. and Reed, S.J.B. (1973) Background corrections for quantitative electron microprobe analysis using a lithium drifted silicon X-ray detector. *Journal of Physics E: Scientific Instruments*, 6, 286–288.
- White, E.W. and Gibbs, G.V. (1969) Structural and chemical effects on the Al K α X-ray emission band among aluminum containing silicates and aluminum oxides. *American Mineralogist*, 54, 931–936.
- Williams, M.L. and Jercinovic, M.J. (2002) Microprobe monazite geochronology: Putting absolute time into microstructural analysis. *Journal of Structural Geology*, 24, 1013–1028.
- Williams, M.L., Jercinovic, M.J., and Terry, M.P. (1999) Age mapping and dating of monazite on the electron microprobe: Deconvoluting multistage tectonic histories. *Geology*, 27, 1023–1026.
- Wing, B.A., Ferry, J.M., and Harrison, T.M. (2003) Prograde destruction and formation of monazite and allanite during contact and regional metamorphism of pelites: Petrology and geochronology. *Contributions to Mineralogy and Petrology*, 145, 228–250.